Journal of Intelligent Material Systems and Structures

Original Article

Journal of Intelligent Material Systems and Structures
2021, Vol. 32(7) 699–723

DOI: 10.1177/1045389X20963188
journals.sagepub.com/home/jim
SAGE

A parametric analysis of the nonlinear dynamics of bistable vibration-based piezoelectric energy harvesters

Luã Guedes Costa[1], Luciana Loureiro da Silva Monteiro[1], Pedro Manuel Calas Lopes Pacheco[1] and Marcelo Amorim Savi[2]

Abstract

Piezoelectric materials exhibit electromechanical coupling properties and have been gained importance over the last few decades due to their broad range of applications. Vibration-based energy harvesting systems have been proposed using the direct piezoelectric effect by converting mechanical into electrical energy. Although the great relevance of these systems, performance enhancement strategies are essential to improve the applicability of these system and have been studied substantially. This work addresses a numerical investigation of the influence of cubic polynomial nonlinearities in energy harvesting systems considering a bistable structure subjected to harmonic excitation. A deep parametric analysis is carried out employing nonlinear dynamics tools. Results show complex dynamical behaviors associated with the trigger of inter-well motion. Electrical power output and efficiency are monitored in order to evaluate the configurations associated with best system performances.

Keywords

Energy harvesting, piezoelectricity, nonlinear dynamics, chaos, bistable systems

1. Introduction

Vibration-based energy harvesting is a concept that has been receiving great attention during the last few decades. In this regard, piezoelectric materials are often employed to convert available mechanical energy into electrical energy due to its unique direct electromechanical coupling properties and its large power density (Erturk and Inman, 2011b). This concept implies a wide variety of applications that depend directly on the scale and the type of the energy harvesting system. Current studies focus on providing a clean and renewable alternative to powering standalone small, micro and nano electronic devices and wireless sensor networks (duToit et al., 2005). But also, on large scales, the available environment mechanical energy is enough to be used as an alternative source of clean energy for urban centers (Toprak and Tigli, 2014).

One of the major issues of simple piezoelectric energy harvesters (PEHs) is the short frequency bandwidth. The maximum performance of these devices is achieved only at vibration frequencies closer to its natural frequency. This causes a limitation in real applications and is only useful in specific situations where there is no considerable variations in the vibration frequency. Although it is possible to tune the natural frequency to the external vibration frequency by adding a proof mass (Kim et al., 2010; Kim and Kim, 2011), this does not counteract the problem, since this method is unable to implement real-time tunable stiffness under time-varying excitation frequency.

In order to widen the bandwidth of the PEHs, several types of nonlinear systems have been proposed. Typical nonlinear PEHs depicted in the literatura are monostable or bistable piezoelectric buckled beams (Cottone et al., 2012; Liu et al., 2013, 2016, 2017; Qian et al., 2020), monostable and bistable piezomagnetoelastic systems (Erturk and Inman, 2011a; Paula et al., 2015; Sebald et al., 2011; Wang et al., 2018b), tristable piezomagnetoelastic systems (Haitao et al., 2015; Kim and Seok, 2015; Zhu et al., 2017), and nonsmooth systems with mechanical stoppers (Ai et al., 2019; Blystad

[1]Department of Mechanical Engineering, Centro Federal de Educação Tecnológica Celso Suckow da Fonseca, CEFET/RJ, Rio de Janeiro, Brazil
[2]Department of Mechanical Engineering, Universidade Federal do Rio de Janeiro, COPPE, Center for Nonlinear Mechanics, Rio de Janeiro, Brazil

Corresponding author:
Marcelo Amorim Savi, Department of Mechanical Engineering, Universidade Federal do Rio de Janeiro, COPPE, Center for Nonlinear Mechanics, P.O. Box 68.503, Rio de Janeiro 21.941.972, Brazil.
Email: savi@mecanica.ufrj.br

and Halvorsen, 2011; Liu et al., 2012). Recent studies also show the development of quadstable and pentastable structures (Kim and Seok, 2014; Wang et al., 2018a; Zhou et al., 2017a, 2017b). Despite many options available to extend the frequency bandwidth and enhance performance of PEHs, each configuration has its advantages and disadvantages. Monostable systems are one of the simplest nonlinear system to be employed, increasing the bandwidth when compared to the linear counterpart, nevertheless presents poor performance when subjected to random excitations, limiting real application options. Nonsmooth systems with mechanical stoppers are capable to vastly enhance frequency bandwidth, however, in return, it presents a decrease in the output power peak due to impact energy loss. In addition, it is subjected to mechanical wear in long-term applications. Bistable systems can present high amplitude responses and better performance for random excitations, being one of the simplest methods to achieve high power performance within a wide range of frequencies, however it requires a prior knowledge of the environment excitation levels due to the existence of a energy barrier intrinsic to the system that prevent the achievement of high amplitude responses with relatively low excitation magnitudes. Tri-, quad- and pentastable PEHs, can also have the same or even slightly higher performances as bistable counterparts due to shallower energy barriers that enable the system to reach high amplitude levels with lower excitation magnitudes. On the other hand, by increasing the number of stable points in the system, more complex, expensive and sensitive it becomes, making it harder to set up precisely (Tran et al., 2018; Yildirim et al., 2017).

This work focuses on the analysis of bistable energy harvesting systems that can be modeled by cubic polynomial stiffness models. There are few ways to induce bistability in a PEH system. The most common approaches found in the literature are the use of magnet interactions and post-buckling configurations. Figure 1(a) shows an illustration depicting the device architecture based on the magnetoelastic structure investigated by Moon and Holmes (1979) and applied to energy harvesting by Erturk et al. (2009) that induce bistability by adding two magnets that interact with the ferromagnetic substructure of a cantilevered beam. Another similar method to produce bistability was investigated by several authors (Andò et al., 2010; Ferrari et al., 2010; Lin and Alphenaar, 2010; Stanton et al., 2010, 2012) and it is illustrated in Figure 1(b). This configuration uses magnetic repulsion phenomenon to create a local instability at the central position, generating 2 stable equilibrium states. Figure 1(c) shows a configuration studied by Zhou et al. (2014) and Kumar et al. (2015, 2017) that uses three magnets and can be set up to have monostability, bistability or tristability depending on the distances between the three magnets.

Buckled configurations can exhibit monostability or bistability and its directly dependent of the buckling force applied. There are two common forms of piezo buckled beam systems. The first was investigated by Masana and Daqaq (2011) and is made by a simple composite beam as shown in Figure 2(a). The second is similar, adding a central proof mass to increase the inertia, changing the natural frequency of the system. It was first experimentally investigated by Sneller et al. (2011) and it is illustrated in Figure 2(b).

Regarding the mechanism to convert energy, vibration-based piezoelectric energy harvesting systems are commonly composed by a substructure made by metal or polymers, thin piezoelectric layers and electrodes connected to a circuit, represented in the Figure by a simple resistor (R_l). The generators are excited and the electro-mechanical coupling properties of piezoelectric materials convert the mechanical energy into electrical energy that is collected by the circuit components. Figure 3 shows most simple compositions and circuit connections of PEHs (Erturk and Inman, 2008; Kim and Kim, 2011).

In order to address the best configurations and successfully design a bistable piezoelectric energy harvesting system, a deep parametric analysis is essential. Due to its complex nonlinear dynamics, the definition and classification of different kinds of dynamical responses and behaviors is an essential task that need to be associated with appropriate tools. In this regard, different types of periodic and chaotic responses can be desirable or undesirable depending on the application. Lyapunov exponents is usually an accepted tool to define chaos and the method proposed by Wolf et al. (1985) is a good alternative for these systems. This contribution develops a numerical parametric investigation of bistable vibration-based piezoelectric energy harvesting systems in order to map and quantify different kinds of dynamical responses. Output power and eficiency are monitored in order to evaluate the system performance. A methodology correlating the intensity of inter-well motion, the amount and efficiency of the energy converted is employed. Results show useful information for energy harvester design based on dynamical analysis.

2. Physical modeling

Bistable energy harvesting systems can be modeled considering a mechanical system connected to an electrical circuit through a piezoelectric element. The devices illustrated in Figures 1 and 2 can be reduced to a single degree of freedom (S-DOF) oscillator shown in Figure 4, with an equivalent mass (m_{eq}), a linear viscous damping coefficient (c), and a nonlinear Duffing-type stiffness ($k(u) = a + bu^2$) resulting from the effects of

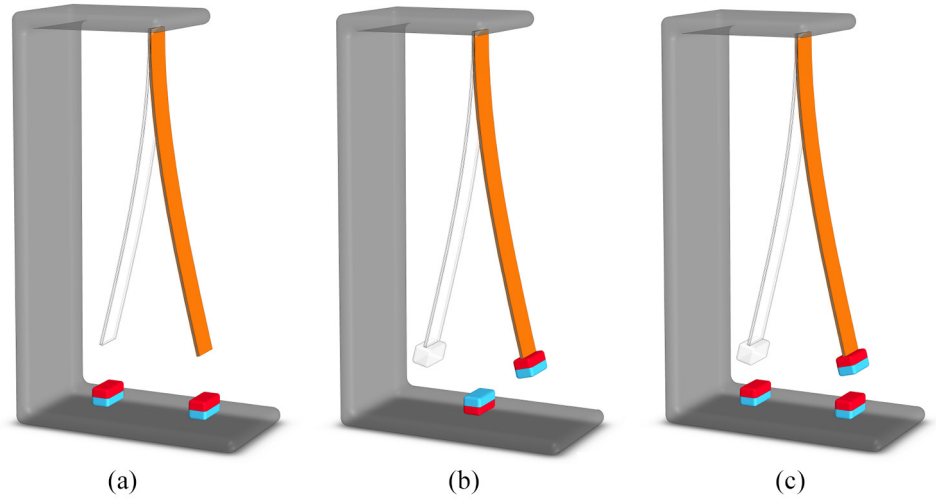

Figure 1. Bistable piezomagnetoelastic systems: (a) with two base magnets and a ferromagnetic substructure beam, (b) with a base magnet and a tip magnet in repulsive configuration, and (c) with two base magnets and a tip magnet in attractive configuration.

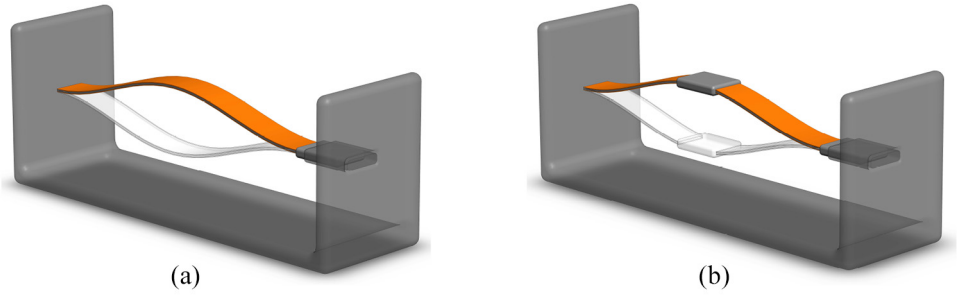

Figure 2. Bistable piezoelectric buckled beam systems: (a) without proof mass, and (b) with proof mass.

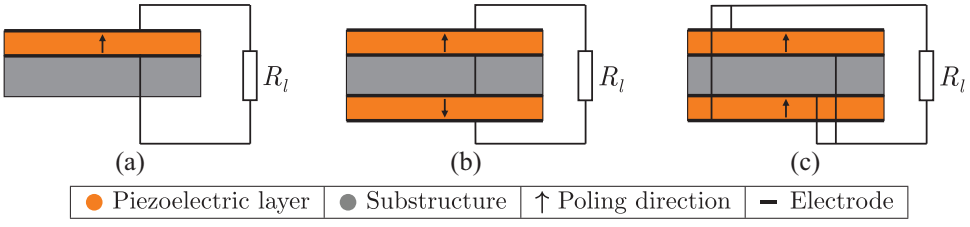

Figure 3. Piezoelectric energy harvesters compositions: (a) unimorph with series connection, (b) bimorph with series connection, and (c) bimorph with parallel connection.

magnetic interaction (for PEH piezomagnetoelastic configurations) or from the effects of the axial compression force on a buckled beam (for piezo buckled beam configuration). The oscillator has the stimulus of a base excitation represented by $u_b(t)$ that generates an equivalent mass displacement, $u(t) = z(t) - u_b(t)$, relative to the base, where $z(t)$ is the displacement of the equivalent mass relative to a inertial referential. The piezoelectric element is connected to an electrical circuit represented by a simple resistive load (R_l). The

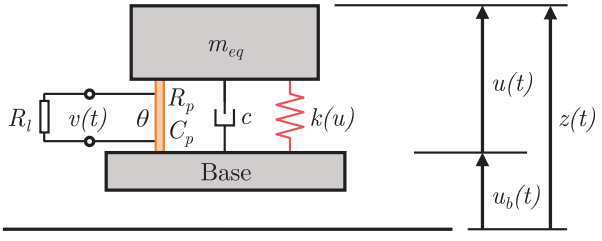

Figure 4. S-DOF lumped model of a bistable vibration based piezoelectric energy harvester.

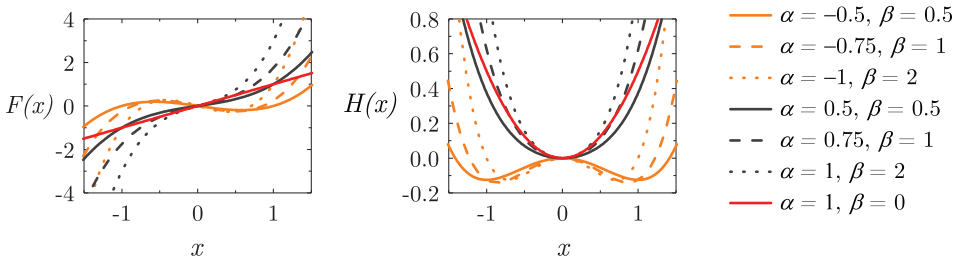

Figure 5. Restitution force and corresponding potential energy for different values of α and β.

mechanical energy of the system is converted into electrical energy by the electromechanical coupling properties of the piezoelectric element with coupling coefficient θ, and the voltage output is represented by $v(t)$.

The equations of motion of the system can be written as a general Duffing-type oscillator with an electromechanical coupling as several authors have shown (Cellular et al., 2018; Cottone et al., 2012; Erturk et al., 2009; Erturk and Inman, 2011a; Ferrari et al., 2010; Kumar et al., 2015, 2017; Liu et al., 2013, 2017; Masana and Daqaq, 2011; Paula et al., 2015; Stanton et al., 2012; Sneller et al., 2011; Zhou et al., 2013):

$$m_{eq}u'' + cu' + f(u) - \theta v = -m_{eq}u_b'' \tag{1}$$

$$\theta u' + C_p v' + \frac{1}{R_{eq}}v = 0 \tag{2}$$

where C_p is the piezoelectric capacitance term and R_{eq} is the equivalent resistance composed by the load resistance (R_l) and the piezoelectric resistance (R_p). The time derivatives are represented by $()'$. Harmonic base excitation is assumed as $u_b = A\sin(\omega t)$, where A and ω are the base displacement amplitude and base displacement frequency, respectively. Therefore $u_b'' = -\omega^2 A\sin(\omega t)$.

The mechanical restitution force of the system is cubic polynomial and is expressed by equation (3), where a and b are the stiffness coefficients.

$$f(u) = k(u)u = au + bu^3 \tag{3}$$

Aiming at a general parametric analysis, working with dimensionless parameters is essential. Consider a reference length (L), a reference voltage (V), a reference frequency of $\omega_0 = \sqrt{|a|/m_{eq}}$, and the following transformations:

$$x = \frac{u}{L}, \quad \dot{x} = \frac{u'}{\omega_0 L}, \quad \ddot{x} = \frac{u''}{\omega_0^2 L} \tag{4}$$

$$\nu = \frac{v}{V}, \quad \dot{\nu} = \frac{v'}{\omega_0 V}, \quad \tau = \omega_0 t \tag{5}$$

$$\zeta = \frac{c}{2m_{eq}\omega_0}, \quad \alpha = \frac{a}{m_{eq}\omega_0^2}, \quad \beta = \frac{bL^2}{m_{eq}\omega_0^2} \tag{6}$$

$$\chi = \frac{\theta V}{m_{eq}\omega_0^2 L}, \quad \kappa = \frac{\theta L}{C_p V}, \quad \varphi = \frac{1}{R_{eq}C_p\omega_0} \tag{7}$$

$$\Omega = \frac{\omega}{\omega_0}, \quad \gamma = \Omega^2\frac{A}{L} \tag{8}$$

Equations (1) and (2) can be rewritten in dimensionless form as:

$$\ddot{x} + 2\zeta\dot{x} + \alpha x + \beta x^3 - \chi\nu = \gamma\sin(\Omega\tau) \tag{9}$$

$$\kappa\dot{x} + \dot{\nu} + \varphi\nu = 0 \tag{10}$$

where x and ν are the new dimensionless spatial coordinate and voltage, respectively; τ is the dimensionless time. The time derivatives of the new coordinates are represented by $(\dot{})$. Therefore, the new dimensionless restitution force of the system is represented by:

$$F(x) = \alpha x + \beta x^3 \tag{11}$$

Stability analysis of the system shows that for $\alpha \geqslant 0$ the system is monostable and has one stable spiral equilibrium point at $(\bar{x}, \dot{\bar{x}}) = (0, 0)$. For $\alpha < 0$ the system is bistable and has two stable spiral equilibrium points and one unstable saddle equilibrium point as shown below:

$$(\bar{x}, \dot{\bar{x}})_1 = \left(-\sqrt{-\frac{\alpha}{\beta}}, 0\right), \quad (\bar{x}, \dot{\bar{x}})_2 = (0, 0), \quad (\bar{x}, \dot{\bar{x}})_3 = \left(\sqrt{-\frac{\alpha}{\beta}}, 0\right) \tag{12}$$

This analysis can be illustrated by the point of view of the potential energy function, presented in equation (13), that shows a double-well potential for bistable systems and a single-well potential for monostable systems.

$$H(x) = \int F(x)dx = \frac{1}{2}\alpha x^2 + \frac{1}{4}\beta x^4 \tag{13}$$

Figure 5 shows possible curves for the restitution force and the potential energy of the system with different values of α and β. The bottom of the wells in the bistable potential energy curve represent the stable equilibrium points, while the unstable point lies at $x = 0$.

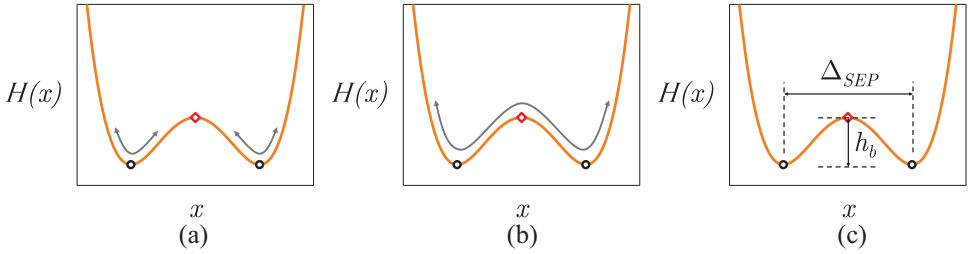

Figure 6. Double well potential for a bistable PEH system showing possible trajetories of motion, the stable equilibrium points (black circles) and the unstable equilibrium point (red diamond): (a) intra-well motion, (b) inter-well motion, and (c) features of interest.

Regarding the performance of the system, it can be evaluated considering the instantaneous dimensionless mechanical power, defined as the product of the velocity by the input excitation:

$$P_{\mathrm{m}} = \dot{x}\gamma \sin(\Omega\tau) \tag{14}$$

and the instantaneous dimensionless electrical power, defined as a product of the voltage by the electrical current:

$$P_{\mathrm{e}} = \nu i = \nu^2 \varphi \tag{15}$$

where $i = \nu\varphi$ is the electrical current. Thus, the overall input (P_{in}) and output (P_{out}) power can be evaluated by the root mean square value (RMS) defined by the following equations:

$$P_{\mathrm{in}} = \sqrt{\frac{1}{\tau}\int_0^{\tau} P_{\mathrm{m}}^2 \, d\tau} \approx \sqrt{\frac{1}{N_p}\sum_{i=1}^{N_p} P_{\mathrm{m}_i}^2} \tag{16}$$

$$P_{\mathrm{out}} = \sqrt{\frac{1}{\tau}\int_0^{\tau} P_{\mathrm{e}}^2 \, d\tau} \approx \sqrt{\frac{1}{N_p}\sum_{i=1}^{N_p} P_{\mathrm{e}_i}^2} \tag{17}$$

where N_p is the number of points considered in the simulation. Also, the efficiency of the system can be evaluated by:

$$\eta = \frac{P_{\mathrm{out}}}{P_{\mathrm{in}}} \tag{18}$$

The following analysis deals with the properties of the potential energy curve of the system. Then, a deep qualitative dynamical analysis is carried out considering the mechanical parameters, the dynamical phenomena and the performance of bistable systems.

3. Potential energy curve analysis

Bistable systems are related to a double-well potential, being associated with negative values of parameter α. The existence of two wells in the potential energy curve implies that the system can either oscillate around one stable equilibrium point presenting intra-well motion, or jump between two wells presenting inter-well motion. In this regard, to exhibit inter-well motion the system has to overcome the potential barrier h_b. Figure 6 illustrates both behaviors and shows features of interest of the energy potential curve.

As showed in Figure 5, the stiffness parameters α and β define the shape of the potential energy curve, $H(x)$. Two parameters are relevant to analyze: the potential energy barrier (h_b) and the distance between stable equilibrium points (Δ_{SEP}). Figure 7(a) shows the potential energy barrier analysis. Purple color region (medium-higher relative values of β and α) represents the lowest energy required to overcome the potential energy barrier and present inter-well motion. For relative lower values of α and β, in red, is the region with higher h_b.

The analysis of the distance between stable equilibrium points (Δ_{SEP}) is important since it determines the scale of the system. Lower values of α and β make Δ_{SEP} wider, and higher values make Δ_{SEP} narrower, as shown in Figure 7(b).

4. Dynamical analysis

In this section, numerical simulations are carried out employing fourth-order Runge-Kutta method to build dynamical maps that identify different kinds of dynamical responses of the system. Poincaré maps are used to classify periodic and aperiodic regions, while Lyapunov exponents are employed to identify chaotic responses. The methodology to build the maps considers initial conditions associated with the rest at a stable equilibrium point, $(x_0, \dot{x}_0, \nu_0) = (\sqrt{-\alpha/\beta}, 0, 0)$ and a specific range of reference values for α and β previously observed in the literature (Cellular et al., 2018; Erturk et al., 2009; Ferrari et al., 2010; Paula et al., 2015). For each combination of values of α and β, a total of 1000 forcing periods are analyzed, considering the last 250 of those as steady-state regime. The resolution of the maps is of 501×501 pixels. Table 1 shows all the parameters employed in the simulations presented in

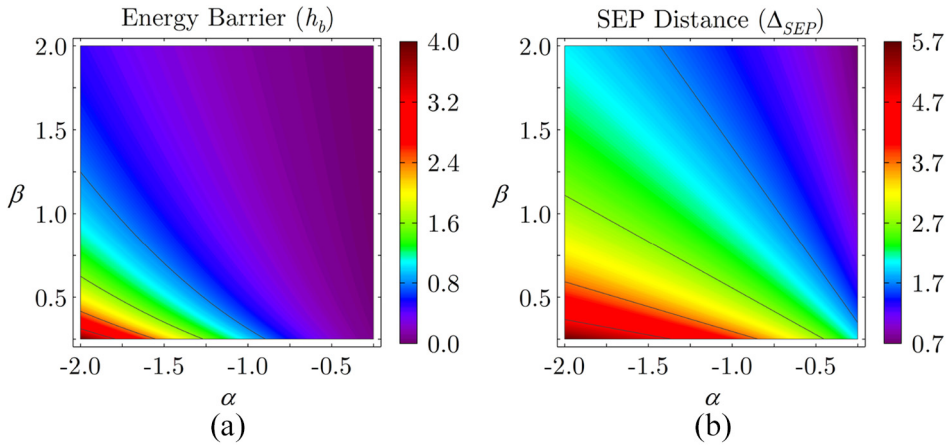

Figure 7. (a) potential energy barrier (h_b), and (b) distance between stable equilibrium points (Δ_{SEP}).

Table 1. System parameter ranges employed for the parametric analysis.

ζ	α	β	γ	Ω	χ	κ	φ
0.025	$-2 \rightarrow -0.25$	$0.25 \rightarrow 2$	$0.01 \rightarrow 1$	$0.01 \rightarrow 2$	0.05	0.5	0.05

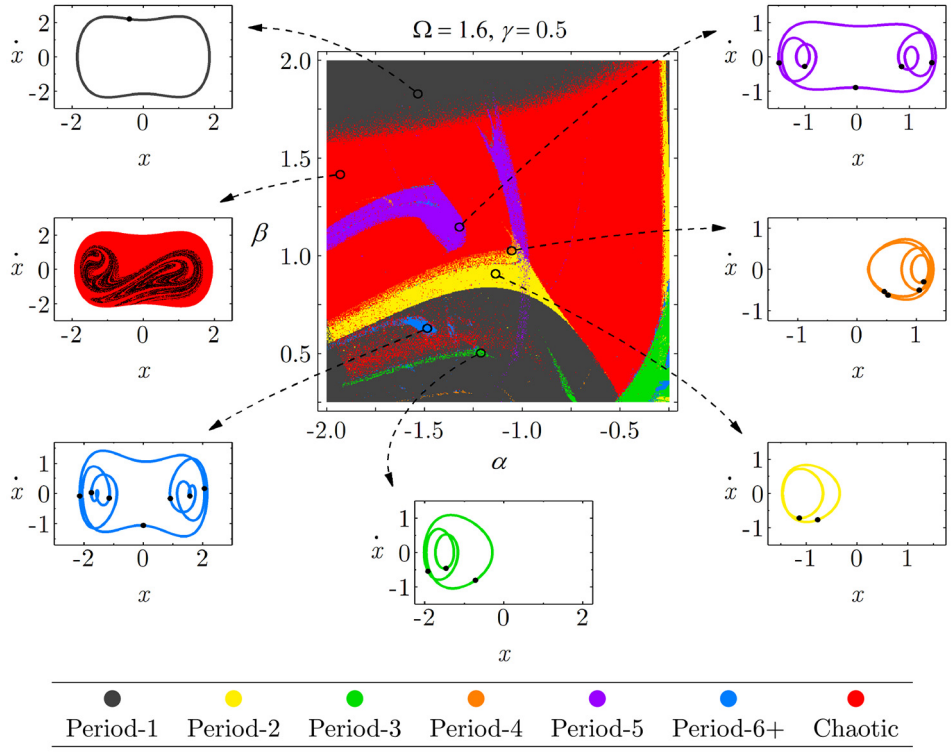

Figure 8. Dynamical response map, local phase spaces and Poincaré maps.

sections "Dynamical analysis," "Output power and efficiency analysis," "Qualitative general analysis," and "Influence of the intensity of inter-well motion and dynamical responses."

Figure 8 shows a dynamical response map for fixed values of $\Omega = 1.6$ and $\gamma = 0.5$. Different colors represent different dynamical responses, identified by a legend in the Figure. Phase space and Poincaré maps

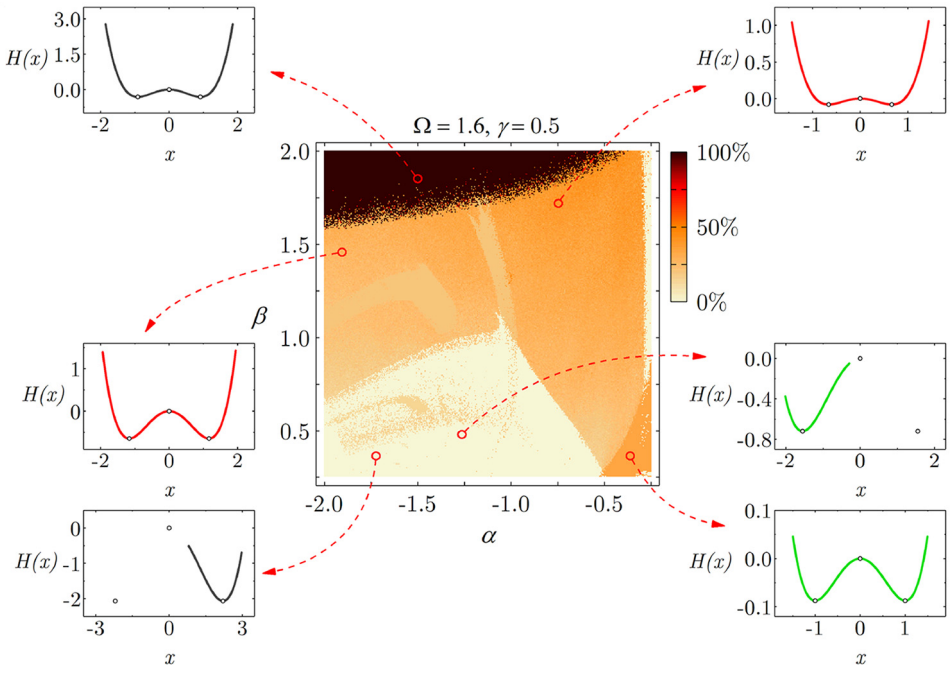

Figure 9. Inter-well motion map and local potential energy curves.

are used to illustrate each response at specific points: period-1 at $(\alpha,\beta)_{1a} = (-1.5, 1.8)$; period-2 at $(\alpha,\beta)_2 = (-1.15, 0.9)$; period-3 at $(\alpha,\beta)_{3a} = (-1.2, 0.5)$; period-4 at $(\alpha,\beta)_4 = (-1.05, 1.04)$; period-5 at $(\alpha,\beta)_5 = (-1.39, 1.16)$; period-6 +, meaning that it has a periodicity equal or greater than 6, at $(\alpha,\beta)_{6+} = (-1.5, 0.63)$; and chaotic at $(\alpha,\beta)_{Ca} = (-1.9, 1.4)$.

Although it is important to identify different kinds of dynamical responses, this information is not enough to fully describe the dynamics of a bistable system. It is important to know if the system exhibits intra-well or inter-well motion. In this regard, inter-well motion maps are built to identify if the system produces intra-well, partial inter-well or full-inter-well motion. In addition, they show the occurrence of dynamical jumps between equilibrium points within a inter-well motion ($IW(\%)$). Figure 9 shows a inter-well motion map for fixed values of $\Omega = 1.6$ and $\gamma = 0.5$. Color legend shows IW: the darker color represents a situation when the system always jumps between wells exhibiting full inter-well motion; on the other hand, the lighter color means that the system does not jump and therefore, exhibits intra-well motion. Colors in between represent the ratio that inter-well motion occurs. As Figure 9 shows, the situation change depending on the region of the map and the type of dynamical response.

Potential energy curves of specific points of the inter-well map show examples of situations where the system can exhibit the same type of dynamical response and different well-motion. Potential energy curves color represent the type of the dynamical response (as depicted in the legend of Figure 8) and black circles represent the equilibrium points. The point $(\alpha,\beta)_{1a} = (-1.5, 1.8)$, one of the analyzed before, features period-1 response with a full ($IW = 100\%$) inter-well motion, while the point $(\alpha,\beta)_{1b} = (-1.7, 0.35)$ features a intra-well ($IW = 0\%$) period-1 response. Another example lies at $(\alpha,\beta)_{3a} = (-1.2, 0.5)$, that exhibits a intra-well period-3 response, while at $(\alpha,\beta)_{3b} = (-0.35, 0.35)$ a period-3 response occurs with a 33.2% partial inter-well motion. The last example considers $(\alpha,\beta)_{Ca} = (-1.9, 1.4)$, exhibiting a chaotic response with 29.8% partial inter-well motion, while $(\alpha,\beta)_{Cb} = (-0.75, 1.7)$ exhibits a chaotic response with 34.6% partial inter-well motion.

In order to further illustrate the behaviors of the system, Figure 10 shows time series of $(\alpha,\beta)_{1b}$, $(\alpha,\beta)_{Ca}$, and $(\alpha,\beta)_{1a}$, showing intra-well motion, 29.8% partial inter-well motion and full inter-well motion, respectively.

A sweep of the excitation frequency is considered over a rage of $\Omega = 0.1$ to $\Omega = 2.0$. Constant values for the excitation amplitude of $\gamma = 0.15$ and $\gamma = 0.5$ are chosen. From Figures 11 and 12, it is observed that there are dynamical response patterns, intrinsic to the system, that have their shape modified depending on the input excitation. The increase of excitation frequency, Ω, makes such patterns to have an expansion and a shift to the top of the map. On the other hand, the increase of the excitation amplitude, γ, makes the patterns to have a contraction and shift to the bottom of the map. These phenomena can be observed in $\Omega = 0.9 \rightarrow 1.3$ maps in Figure 11, in which there is an enlargement of the patterns towards the top of the map. The contraction is observable, for example, by

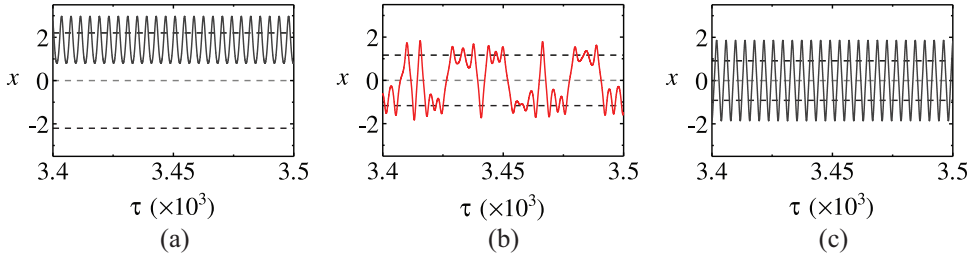

Figure 10. Time series of: (a) period-1 response with intra-well motion, (b) chaotic response with 29.8% partial inter-well motion, and (c) period-1 response with full inter-well motion. Dashed lines represent equilibrium points.

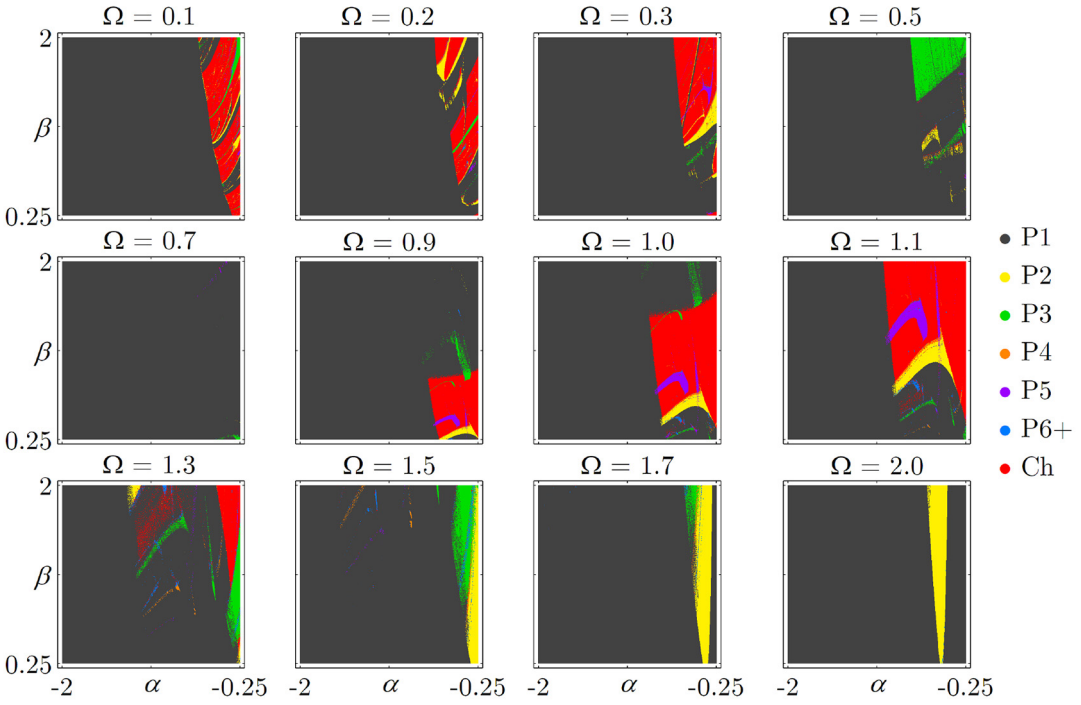

Figure 11. Dynamical response maps over a range of $\Omega = 0.1 \rightarrow 2.0$ with a constant value of $\gamma = 0.15$.

comparing $\Omega = 1.3$ Map in Figure 11 with the equivalent one in Figure 12, in which a reduction occurs in the patterns towards the bottom of the map. P# and Ch in graph legend are abbreviations for Period and Chaotic, respectively.

For the same parameters, Figures 13 and 14 present inter-well motion maps. It is observed that the dynamical patterns also retain its well motion characteristics. In addition, there is a downward trend of full inter-well motion for higher values of Ω. It can be observed that with the increase of frequency, there is an increase in the area of full inter-well motion, until it reaches a limit and starts to decrease. Besides, there is a trend to increase the full inter-well motion for higher values of γ, as expected. It can be observed that the increase of γ enlarges the area of full inter-well motion of the maps and makes it appears in a wider range of frequencies. This phenomenon is associated with a broader bandwidth of the system when subjected to higher base displacement amplitudes.

By comparing Figures 13 and 14 with Figure 7(a) it is also evident that inter-well motion is more recurring at regions of lower potential energy barrier. In addition, in neither case the region of higher potential energy barrier presents inter-well motion.

The need for two types of maps in the dynamical analysis is also highlighted in some cases. The most explicit ones occur when $\gamma = 0.15$, $\Omega = 0.7$, and $\gamma = 0.5$, $\Omega = 1.0$. It is observed the majority of the dynamical response map's area as a period-1 response, while at inter-well motion maps, it shows two distinct regions of intra-well motion and full inter-well motion.

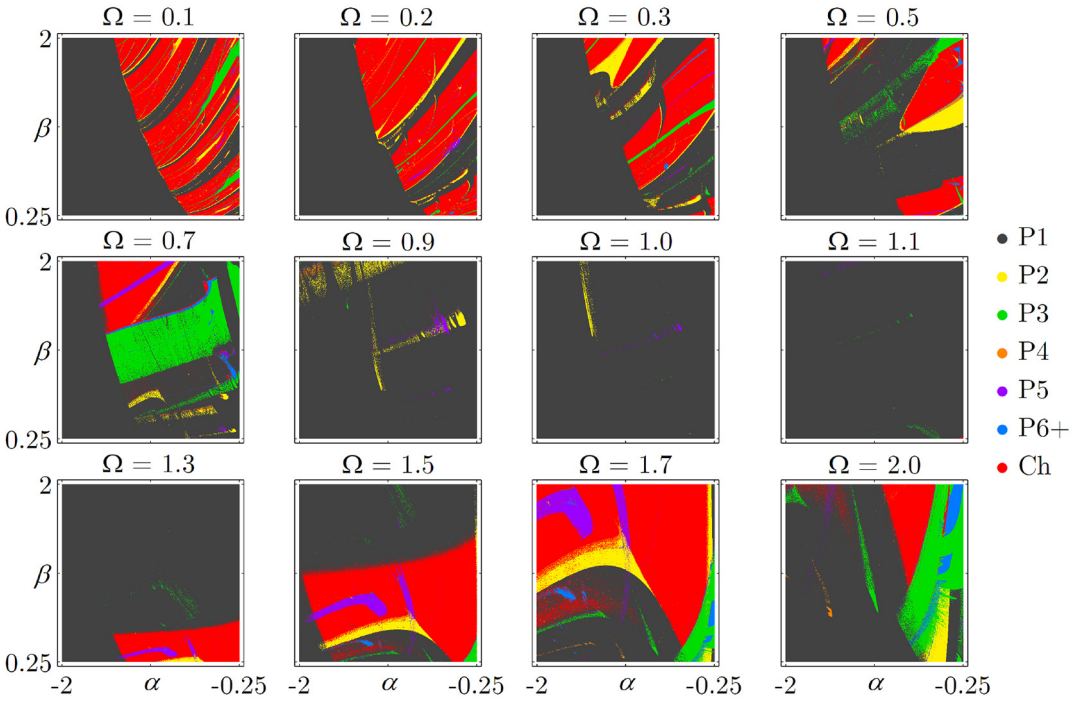

Figure 12. Dynamical response maps over a range of $\Omega = 0.1 \rightarrow 2.0$ with a constant value of $\gamma = 0.5$.

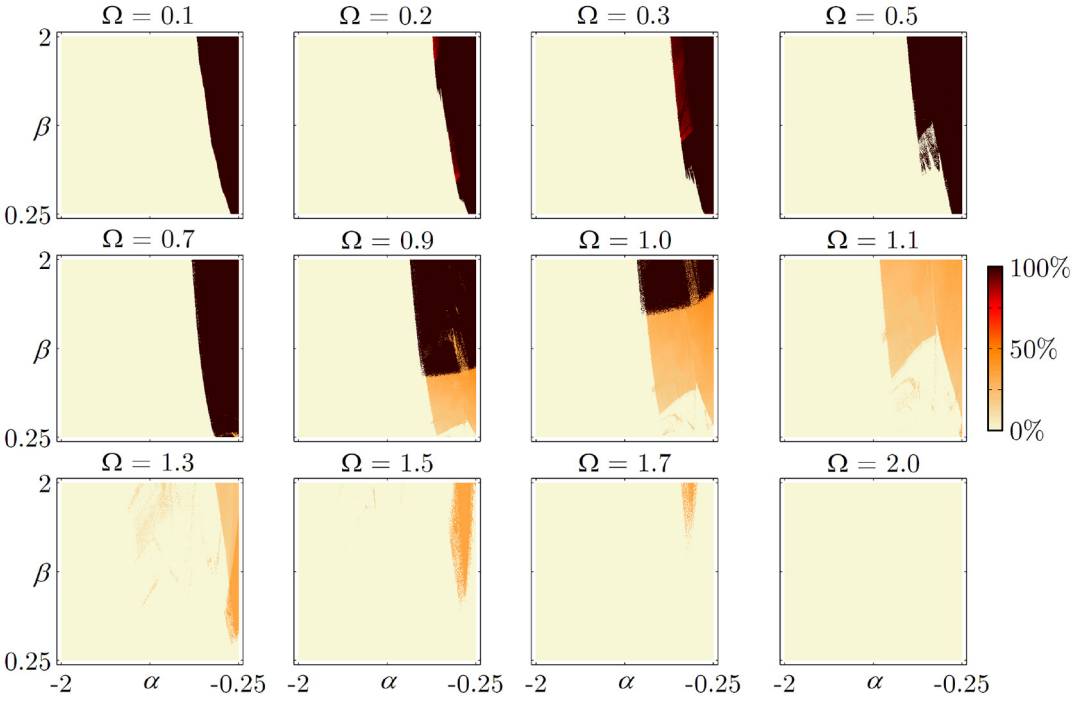

Figure 13. Inter-well motion maps over a range of $\Omega = 0.1 \rightarrow 2.0$ with a constant value of $\gamma = 0.15$.

5. Output power and efficiency analysis

In this section, numerical simulations are carried out employing the same procedure and parameters described in section "Dynamical analysis" to build power output maps and efficiency maps for evaluation of the converted energy by the system. The output power and efficiency of the system at each point of the

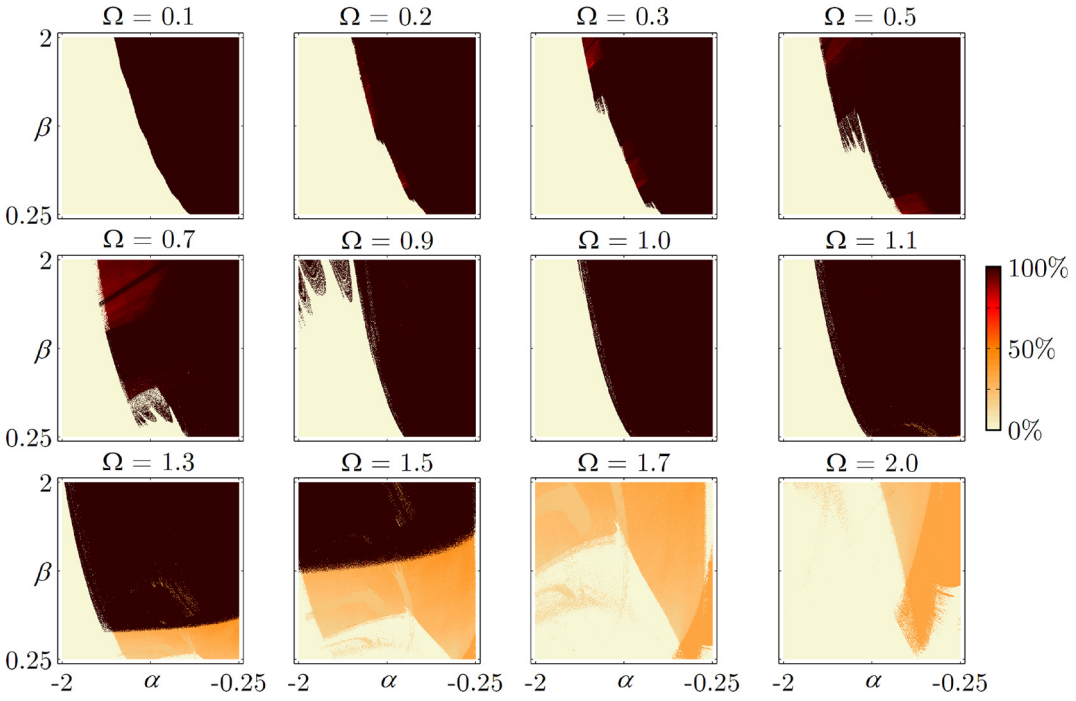

Figure 14. Inter-well motion maps over a range of $\Omega = 0.1 \rightarrow 2.0$ with a constant value of $\gamma = 0.5$.

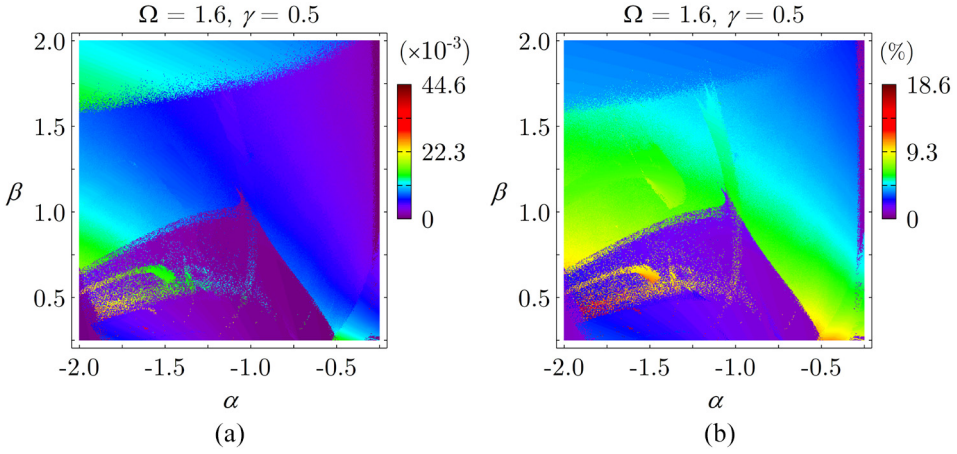

Figure 15. (a) power output map, and (b) efficiency map.

maps are calculated by equations (17) and (18), respectively.

Figure 15 shows an output power (P_{out}) map and an efficiency (η) map for constant values of $\Omega = 1.6$ and $\gamma = 0.5$. In both cases, red represents the highest values and dark purple represents the lowest values. It can be noticed, when compared with Figure 9, that higher output power is achieved in cases where the system exhibit inter-well motion than in cases where the system exhibits intra-well motion, as expected. Besides, when comparing Figure 15(a) and (b) it can be observed that the changes of the power output values are not necessarily associated with the change in efficiency. This behavior can be seen in the top left and right regions of the maps. On the top left region an increase of the power output is observed while the efficiency remains relatively the same. On the other hand, the pattern of change of the power at the map right regions does not follow the same pattern of the efficiency change.

Again, a sweep of the excitation frequency is considered over a range of $\Omega = 0.1$ to $\Omega = 2.0$ and constant values of excitation amplitude of $\gamma = 0.15$ and $\gamma = 0.5$

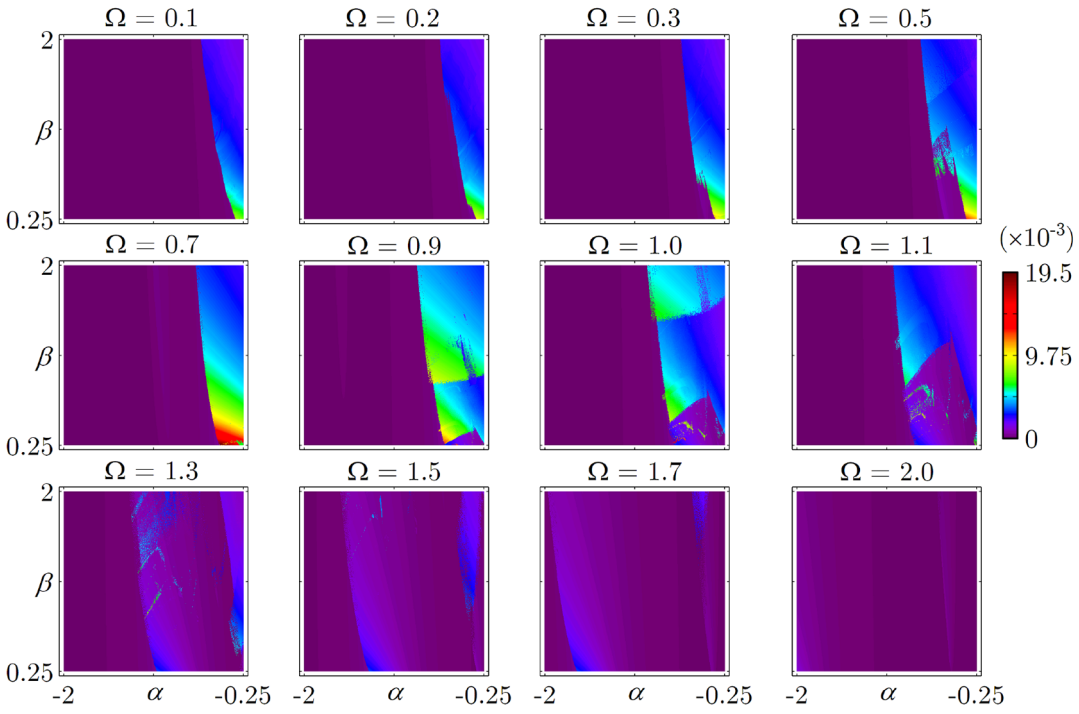

Figure 16. Power output maps over a range of $\Omega = 0.1 \rightarrow 2.0$ with a constant value of $\gamma = 0.15$.

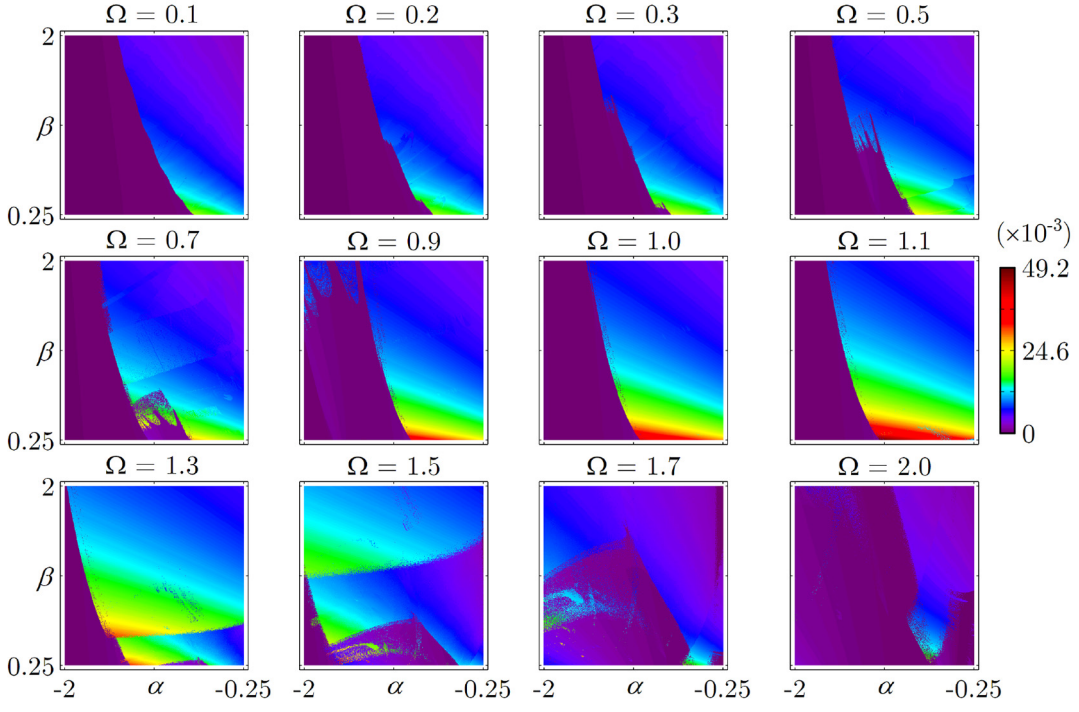

Figure 17. Power output maps over a range of $\Omega = 0.1 \rightarrow 2.0$ with a constant value of $\gamma = 0.5$.

are chosen. It is observed in Figures 16 and 17 that maximum power outputs occur around $\Omega = 0.5$ to $\Omega = 0.9$ for $\gamma = 0.15$ and around $\Omega = 0.9$ to $\Omega = 1.3$ for $\gamma = 0.5$, therefore it is evident that an increase of the forcing amplitude, γ, causes the maximum power output to occur at higher frequencies. Also, the increase of γ expands the output power scale as expected. The maximum value of power output in

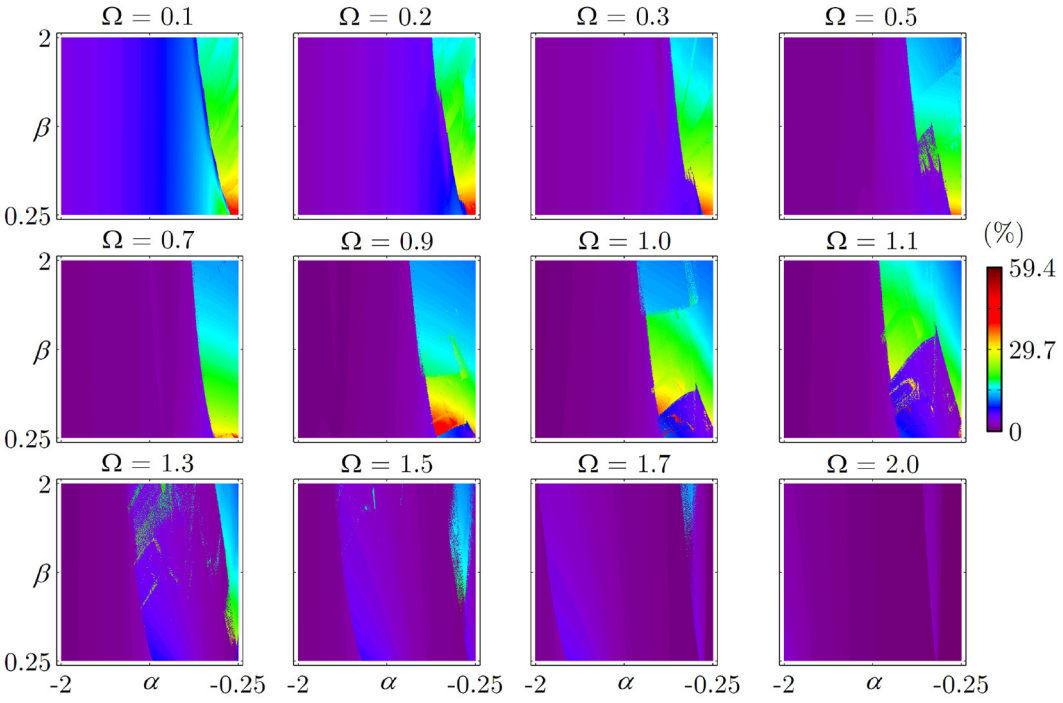

Figure 18. Efficiency maps over a range of $\Omega = 0.1 \rightarrow 2.0$ with a constant value of $\gamma = 0.15$.

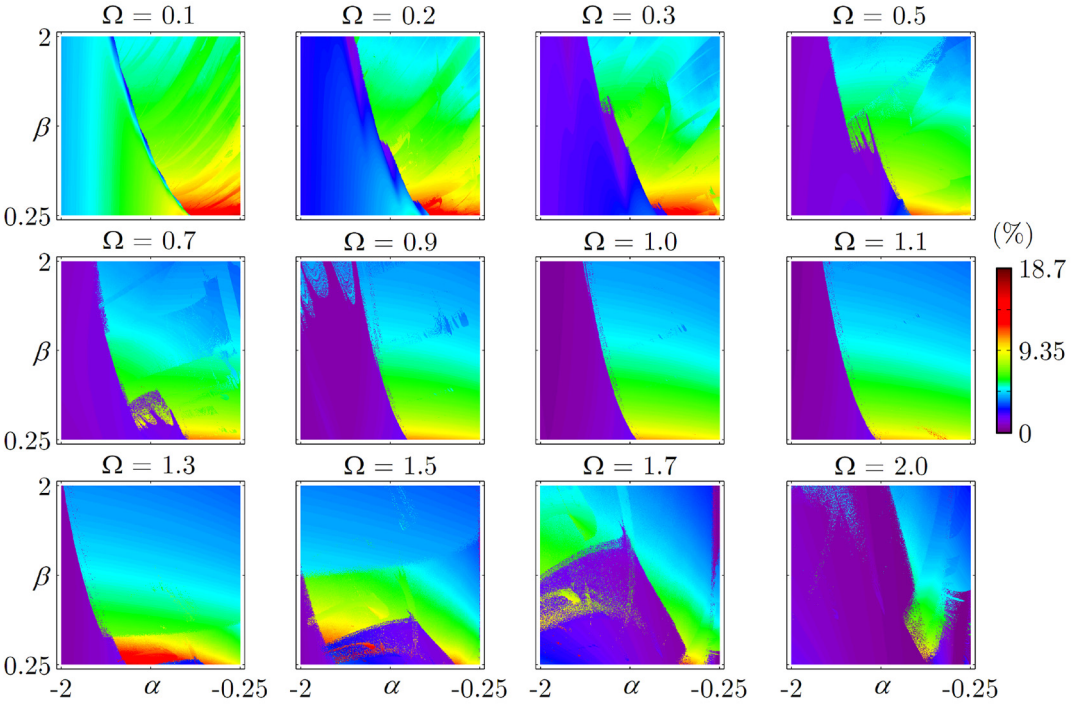

Figure 19. Efficiency maps over a range of $\Omega = 0.1 \rightarrow 2.0$ with a constant value of $\gamma = 0.5$.

Figure 16 is $P_{\text{out}}^{(\max)} = 19.5 \times 10^{-3}$, while in Figure 17 is $P_{\text{out}}^{(\max)} = 49.2 \times 10^{-3}$.

From Figures 18 and 19, it is observed that higher efficiency tends to occur for lower values of β and γ. In addition, the efficiency is also higher at regions that exhibit inter-well motion, in almost all the cases analyzed. The exception occurs in the case that $\Omega = 0.1$, showing regions of intra-well motion with higher efficiencies than some zones of inter-well motion.

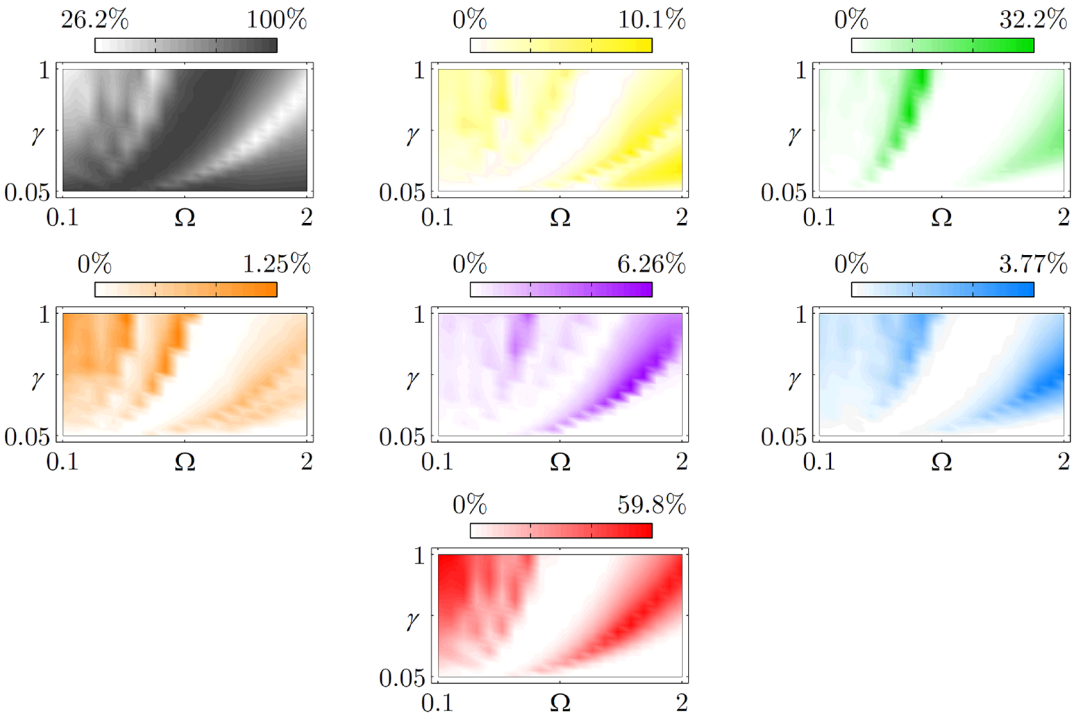

Figure 20. Occurrence percentage of dynamical responses for each combination of γ and Ω.

6. Qualitative general analysis

As observed in sections "Dynamical analysis" and "Output power and efficiency analysis," the system presents a very complex dynamics, exhibiting different responses at each combination of parameters. Moreover, it is very difficult to choose an optimum region for energy harvesting purposes by analyzing only a few specific cases. Therefore, in this section, 400 cases (α versus β maps) are analyzed varying the excitation amplitude from $\gamma_i = 0.05$ to $\gamma_f = 1$ with steps of $\Delta\gamma = 0.05$ and the excitation frequency from $\Omega_i = 0.1$ to $\Omega_f = 2$ with steps of $\Delta\Omega = 0.1$.

In order to determine the most prominent dynamical responses, the percentage of the response occurrence is calculated for each dynamical response map. Figure 20 summarizes these results showing that period-1 (dark gray), chaotic (red) and period-3 (green) responses occur more often than others (note the different percentage scales for each case). It is observed that darker areas of period-1 plot (dark gray) are equivalent to lighter areas of the other plots, showing a total predominance of period-1 responses in these regions. On the other hand, there are specific regions in which the chance of period-2 (yellow), period-3 (green), period-4 (orange), period-5 (purple), period-6 + (blue), and chaotic (red) responses to occur increase, reducing period-1 occurrence. In addition, period-4 (orange), period-5 (purple), and period-6 + (blue) responses occur less often.

Now, by using an overlapping process to compare all the dynamical response maps for all 400 cases and analyzing the influence of the stiffness parameters, α and β, Figure 21 presents the percentage of cases in which the corresponding dynamical response occur. Note that higher values of α exhibit more complex responses (period-2, period-3, period 6 + , and chaotic), while low values of α are associated with a predominant period-1 response, reaching occurrence of 98.8%. Period-4 and period-5 responses have multiple spaced high density regions, filling a larger portion of the map. It is important to be pointed out that each map has its own scale, so the minimum of period-1 response (48.8% occurrence) is still greater than any other. Period-4, period-5 and period-6 + occur at lower rates.

It should be noticed in Figure 20 that each of these color maps presents a similar structure and, in addition, Figure 21 is associated with patterns that repeat over the maps. These two observations indicate an alternative way to observe the process of translation, expansion and contraction of response patterns observed in Figures 11 and 12 of section "Dynamical analysis."

The same procedure done in Figure 20 is applied to analyze the occurrence percentage of inter-well motion for each combination of γ and Ω. From Figure 22, it is observed that as γ increases, the peak occurrence zone of inter-well motion is moved to higher values of Ω. This behavior is connected to the change in frequency in which maximum power occurs when increasing the

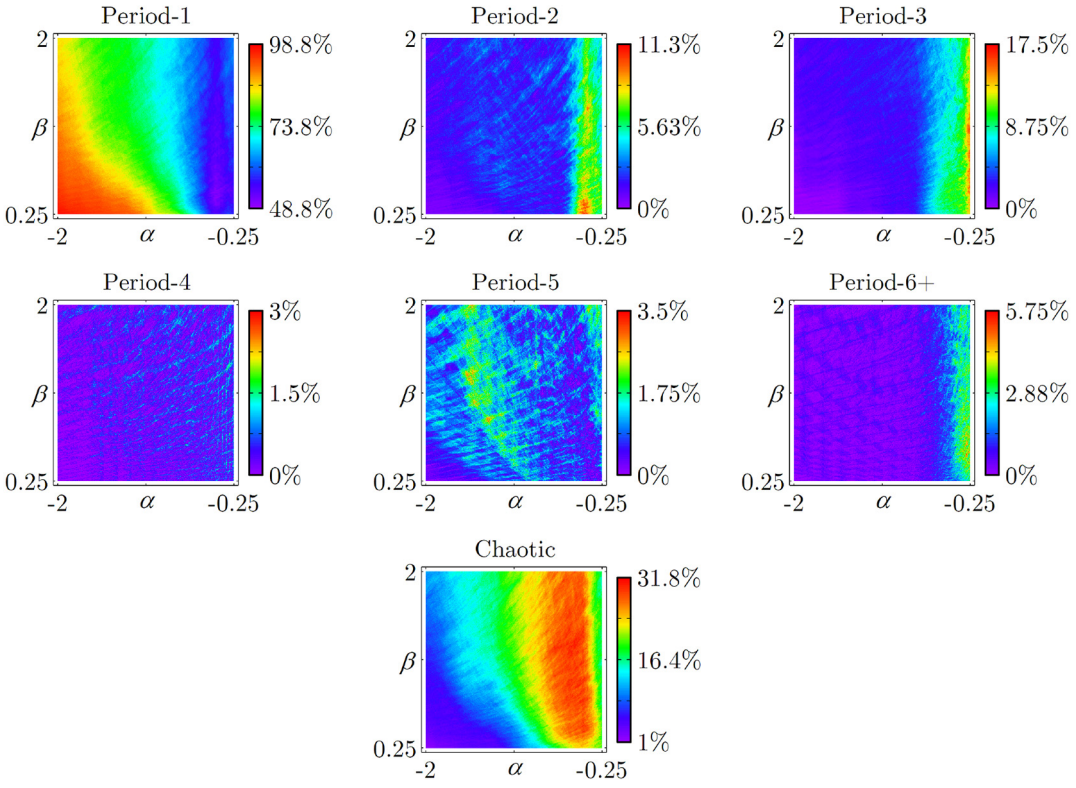

Figure 21. Occurrence percentage of dynamical responses regarding the influence of α and β.

excitation amplitude, as showed in Figures 16 and 17 of section "Output power and efficiency analysis." It also confirms the observations made in Figures 13 and 14 of section "Dynamical analysis."

The overlapping of all 400 cases to compare well-motion maps is presented in Figure 23(a) that shows the region in which general inter-well motion occurs more often. Comparing this result with Figure 7(a), it is evident that smaller potential energy barriers (h_p) provide a higher occurrence of inter-well motion, as expected. Moreover, Figure 23(b) and (c) isolate full and partial inter-well motion occurrences, showing that the partial inter-well motion is more often for mid-lower values of β and higher values of α, while full inter-well occurrence is more usual for higher values of β. Figure 23(d) is the opposite of Figure 23(a), showing intra-well motion, which is undesirable for power conversion, as discussed in section "Output power and efficiency analysis."

In order to present a general analysis of the electrical power output, a normalization of the power is done for each output power map in all the 400 cases before the overlapping process, as each one have a different power scale due to different forcing conditions. Therefore a normalized power (P_{norm}) is defined as

$$P_{\text{norm}} = \frac{P_{\text{out}}}{P_{\text{out}}^{(\max)}} \tag{19}$$

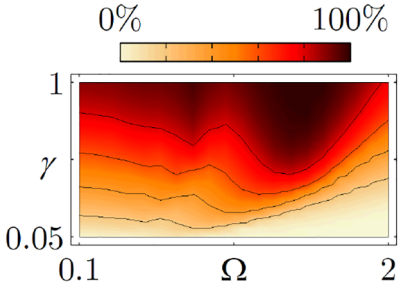

Figure 22. Occurrence percentage of inter-well motion for each combination of γ and Ω.

where P_{out} is the electrical power output at each point of the map and $P_{\text{out}}^{(\max)}$ is the maximum electrical power output of each individual map. By doing this, the scale of the maps is standardized to a range of 0 to 1, enabling a qualitative analysis of the power conversion.

Figure 24 highlights the best regions of power conversion for different reference values of P_{norm}. Thus, for general cases where there is a wide range of forcing parameters, the best setup to get high magnitude power levels is found at values of $\beta < 0.5$ and around $\alpha = -0.75$.

A general analysis of the conversion energy efficiency is now of concern. By comparing the 400 cases

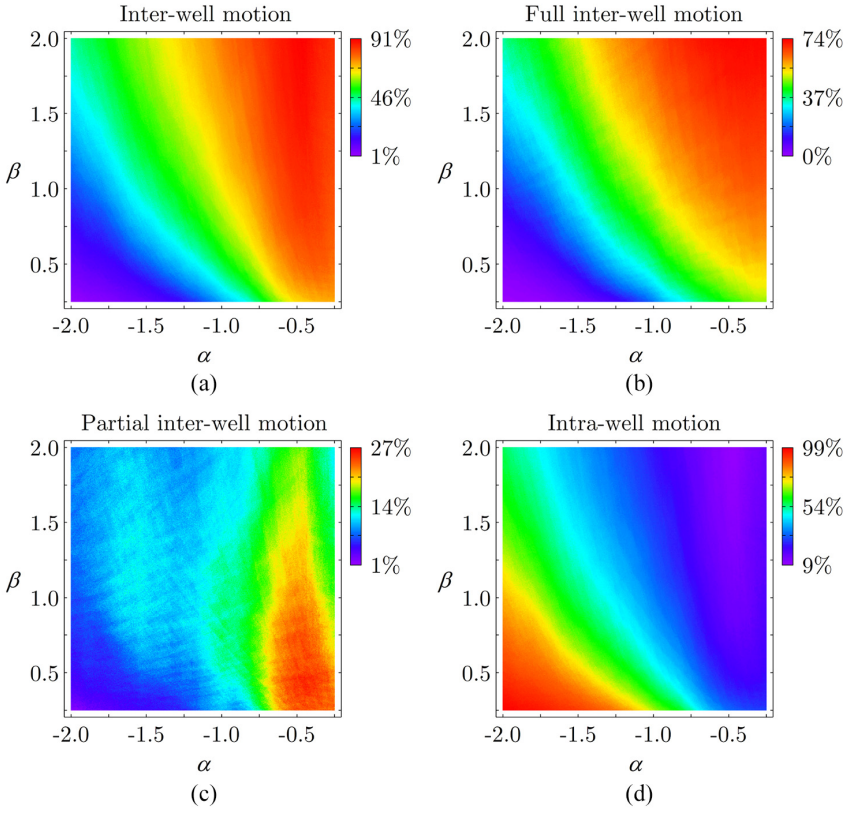

Figure 23. Occurrence percentage of: (a) general inter-well motion, (b) full inter-well motion, (c) partial inter-well motion, and (d) intra-well motion.

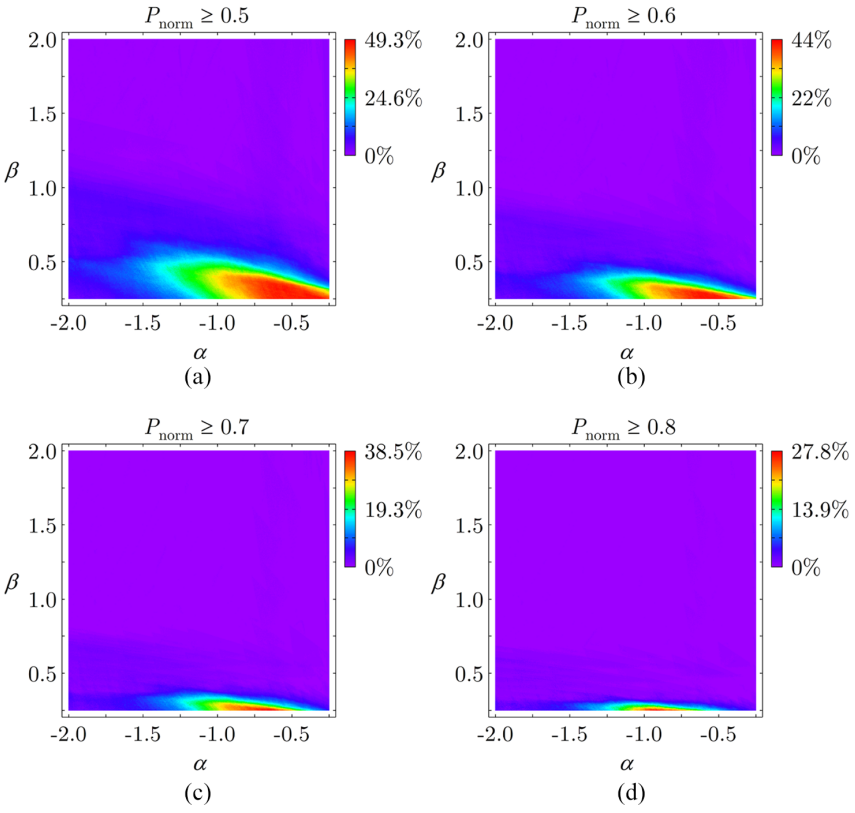

Figure 24. Occurrence percentage of high output power for a reference of: (a) $P_{norm} \geqslant 0.5$, (b) $P_{norm} \geqslant 0.6$, (c) $P_{norm} \geqslant 0.7$, and (d) $P_{norm} \geqslant 0.8$, regarding α and β.

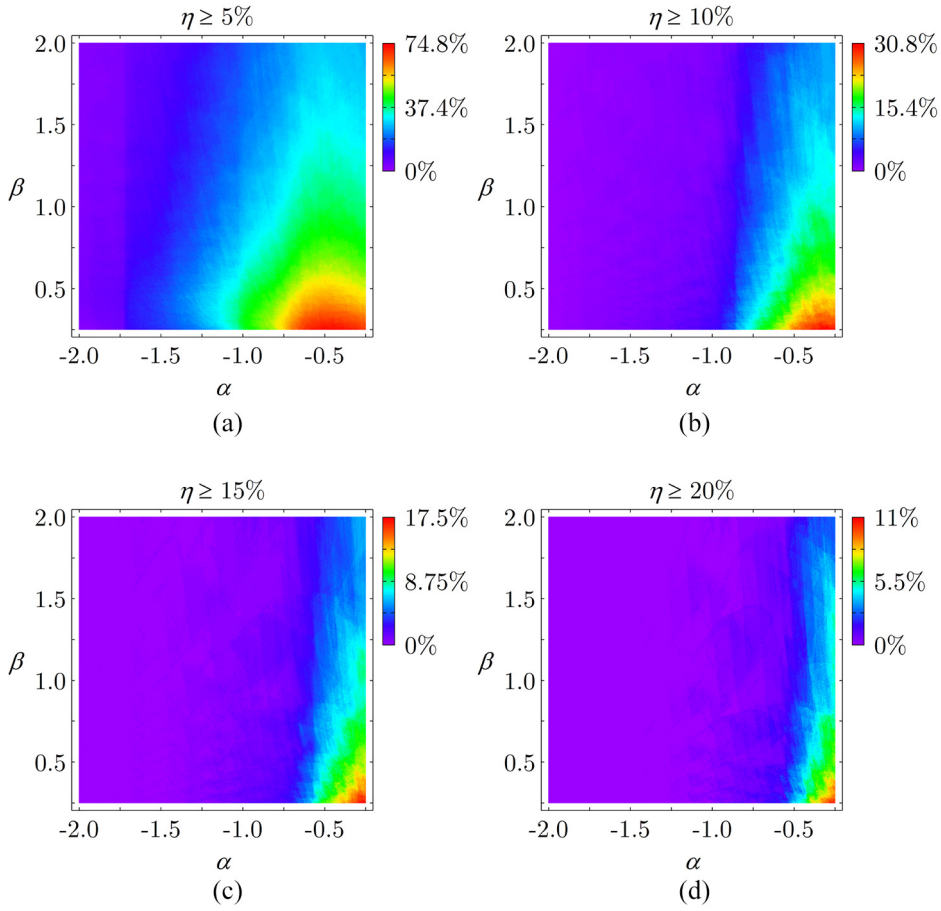

Figure 25. Occurrence percentage of efficiency for a reference of: (a) $\eta \geq 5\%$, (b) $\eta \geq 10\%$, (c) $\eta \geq 15\%$, and (d) $\eta \geq 20\%$, regarding α and β.

previously analyzed and applying the overlapping process, Figure 25 highlights the best regions for different reference values of efficiency (η), showing that the system is more efficient at lower values of β and higher values of α. In order to clarify this conclusion, it should be observed that Figure 25(a) shows that ≈74.8% of the cases in which the efficiency is greater than 5% occurs in the red region.

By comparing Figures 24 and 25, it is noticeable the trend of higher power outputs to occur at bottom regions of the maps, while higher efficiencies occur more times at the right region of the maps. Still, there is a trend of the system to be more efficient at regions of higher power outputs.

Figure 26 shows response, well-motion, output and efficiency maps as a function of Ω and γ, from top to bottom, respectively. Fixed initial conditions are considered for each combination of Ω and γ, respecting the parameters described in Table 1. Local points are chosen for an intermediary reference of $P_{\text{norm}} \geq 0.7$. Figure 26(a) represents a best case scenario for high output power with moderate-size inter-well regions, while Figure 26(b) shows a best case scenario for achieving larger inter-well motion regions with lower excitation magnitudes, however presenting low power output magnitudes. Moreover, Figure 26(c) presents a worst case scenario for inter-well regions and moderate power output magnitudes. In these three examples, larger inter-well regions can be associated with larger bandwidth capacity of the system. It is important to notice that the wider is the bandwidth, the lower is the value of γ required to trigger inter-well motion, but it has a cost of maximum power output magnitude. In addition, high efficiency regions are associated with peak power regions of low values of γ (resonance regions). Furthermore, it is interesting to observe in these dynamical response maps the presence of the same dynamical patterns observed in the α versus β maps. Furthermore, Figure 27 shows the shape of potential energy functions for these cases.

7. Influence of the intensity of inter-well motion and dynamical responses

Comparing all the results presented so far, there is a clear relationship between inter-well motion and high

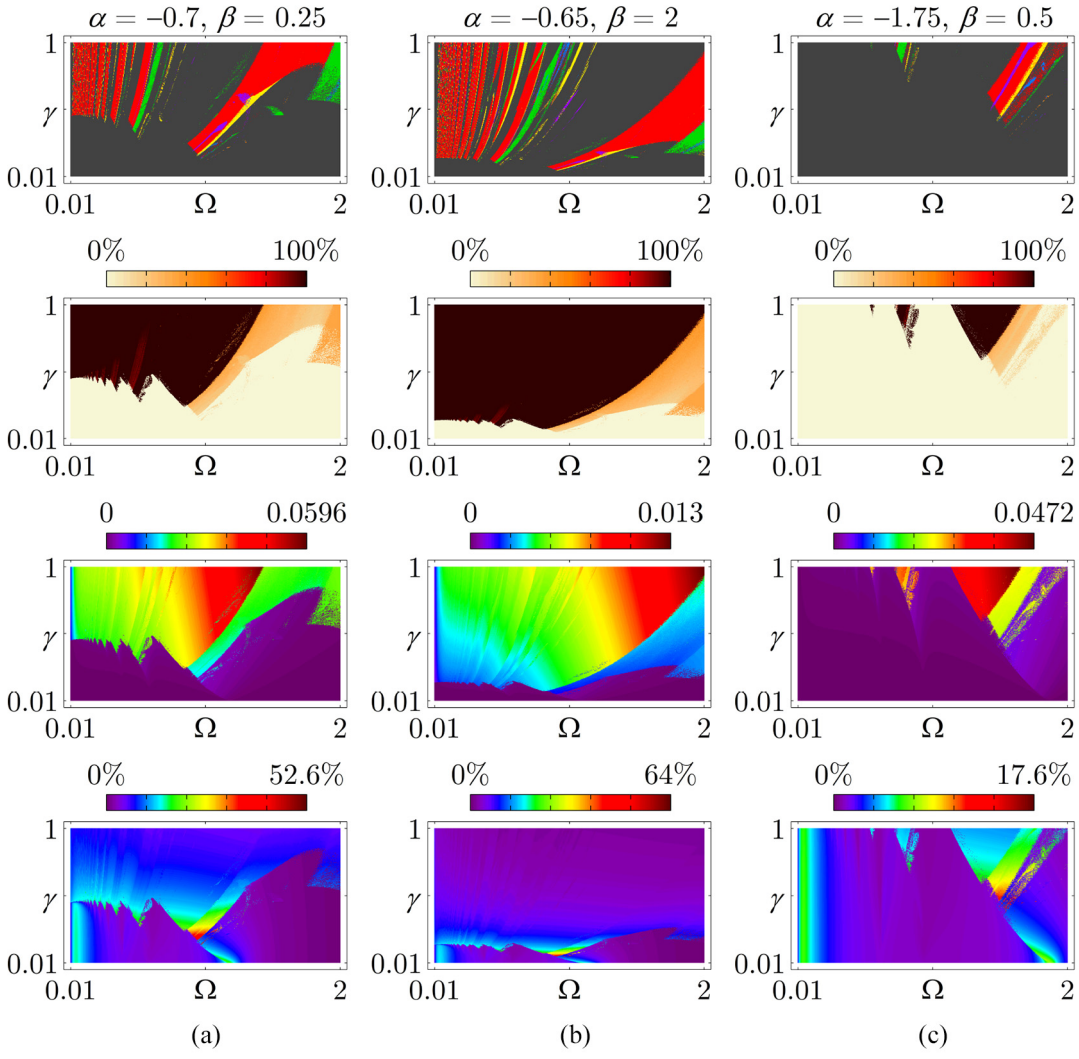

Figure 26. From top to bottom: dynamical, well-motion, power output and efficiency maps regarding Ω and γ for local points of: (a) $(\alpha, \beta) = (-0.7, 0.25)$, (b) $(\alpha, \beta) = (-0.65, 2)$, and (c) $(\alpha, \beta) = (-1.75, 0.5)$.

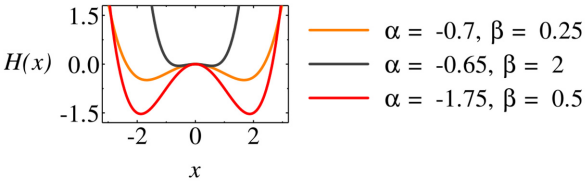

Figure 27. $H(x)$ for best case scenario of P_{out} (orange), for best case scenario of larger bandwidth (dark grey), and worst case scenario for power and bandwidth (red).

capacity of energy conversion, as expected. In addition, only a low energy barrier does not necessarily mean that the system is optimized for energy harvesting in general cases where there is a wide variation of forcing parameters. Moreover, within the scope of the analysis, taking into account the influence of the stiffness parameters, it is inconclusive whether the type of dynamical responses and the intensity of inter-well motion impact the quality of energy conversion. Hence, lets now consider a local point $(\alpha, \beta) = (-0.7, 0.25)$, the same point of Figure 26(a), to measure the influence of those aspects. The same procedure of analysis is implemented and Figure 28 shows response map, output power map and inter-well motion map as a function of Ω and γ.

Areas of interest representing different dynamical behaviors are now in focus. Dashed rectangles represent zoomed areas of interest. Rectangles 1 and 2 represent intra-well motion regions; rectangles 3 and 4 represents partial intra-well regions; and rectangle 5 takes in consideration an area with full inter-well motion. Next subsections cover a careful analysis of the influence of the dynamical responses for each type of well motion

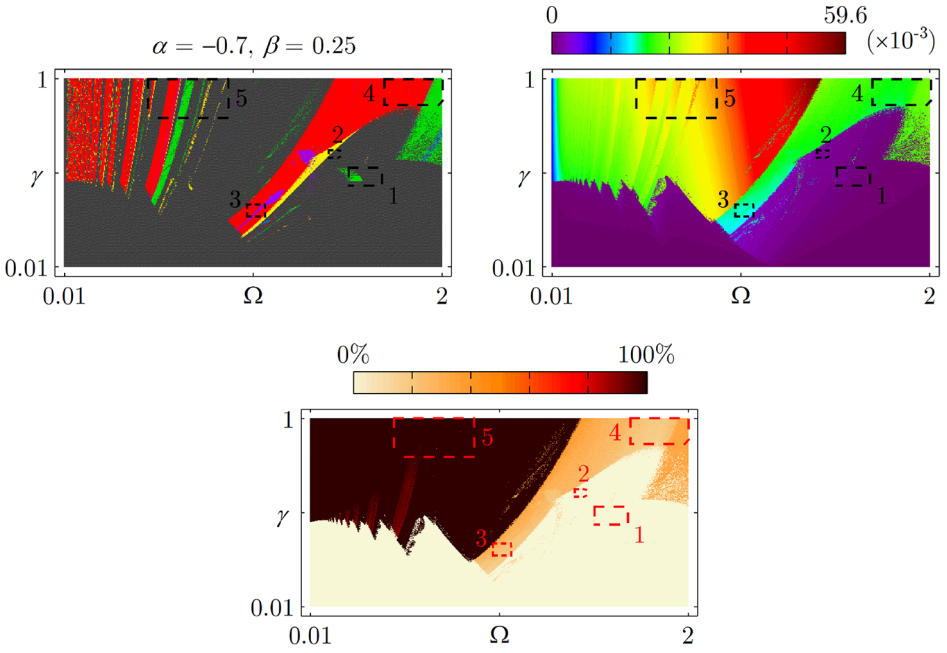

Figure 28. Dynamical response (top left), output power (top right) and inter-well motion (bottom center) maps as a function of Ω and γ for $(\alpha, \beta) = (-0.7, 0.25)$.

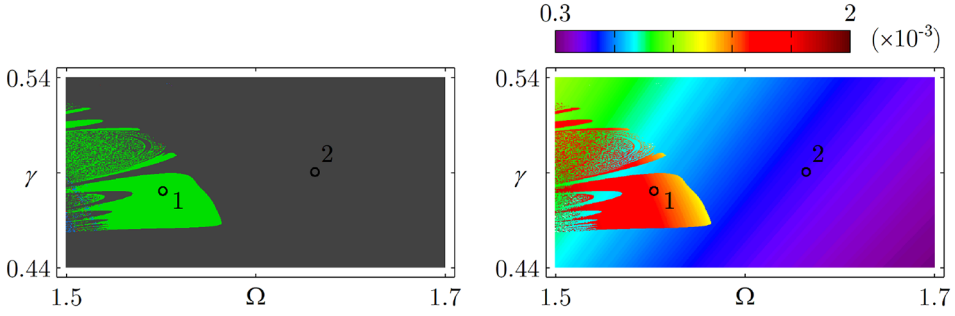

Figure 29. Dynamical response map (left) and output power map (right) as a function of Ω and γ for $(\alpha, \beta) = (-0.7, 0.25)$ at zoomed area 1 (see Figure 28).

behavior in order to understand how the change in dynamical response affects the power output of the system.

7.1. Influence of dynamical responses for intra-well motion

Considering areas of intra-well motion (see Figure 28), a comparison between period-1 and period-3 responses is shown in Figure 29 at zoomed area 1. Two points are selected on the map in order to analyze period-1 (point 1) and period-3 (point 2) areas separately. Table 2 summarizes the information regarding the points analyzed. It is observed that a smooth change in power output occurs as a result of the variation of excitation parameters while inside the same dynamical response. Besides, the abrupt change of dynamical responses causes period-3 point to present ≈180% better performance than period-1 point. It is also observed an erosion of the period-3 motion region, being associated with a fractal-like structure related with different kinds of motions in a close region.

Table 2. Points details of Figure 29.

Point	Response	(Ω, γ)	P_{out}
1	Period-3	(1.55, 0.48)	1.418×10^{-3}
2	Period-1	(1.63, 0.49)	0.506×10^{-3}

Another case is presented in Figure 30, showing zoomed area 2 of Figure 28, presenting a comparison between period-1 and period-2 response areas. As before, there is a smooth change in power output as a result of the influence of the excitation parameters. The abrupt change between responses causes abrupt

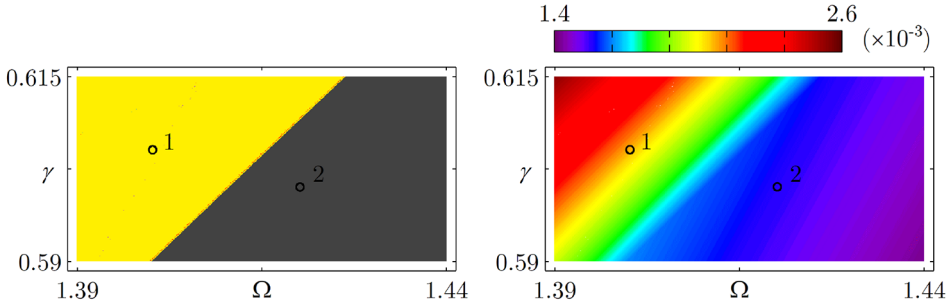

Figure 30. Dynamical response map (left) and output power map (right) as a function of Ω and γ for $(\alpha, \beta) = (-0.7, 0.25)$ at zoomed area 2 (see Figure 28).

Table 3. Points details of Figure 30.

Point	Response	(Ω, γ)	P_{out}
1	Period-2	(1.4, 0.605)	2.07×10^{-3}
2	Period-1	(1.42, 0.6)	1.56×10^{-3}

changes in power output. From point 1 to point 2, there is a ≈32% increase in power output. Table 3 summarizes the information regarding the points analyzed.

7.2. Influence of dynamical responses for partial inter-well motion

The influence of dynamical responses for partial inter-well motion is now in focus. Tables 4 and 5 summarize the information regarding the points analyzed in this subsection. Figure 31 shows zoomed region 3 (see Figure 28) predominantly containing chaotic and period-5 responses. In this case, comparing only the chaotic points, it is observed that the power output has a relation with the intensity of the inter-well motion. For greater intensities, larger power outputs are observed. On the other hand, the abrupt change of chaotic to period-5 response increases the power output, even with lower inter-well motion occurrence.

Figure 32 presents a similar behavior. Points 1 and 2 are chaotic and it's observed an increase in power output as inter-well motion intensity increases. But abrupt changes in the dynamical response from chaotic to periodic causes abrupt changes to inter-well intensity, increasing the power output. Therefore, as abrupt changes in dynamical responses, inter-well intensity also plays an important role regarding the influence in system performance.

7.3. Influence of dynamical responses for full inter-well motion

Considering areas of full inter-well motion, Figure 33 shows the area represented by the 5th dashed square in Figure 28. In this case, abrupt changes in power output also occur if different dynamical response areas are analyzed separately. Still, as the maps show, the complexity of the region and the presence some regions of partial inter-well motion requires to discretize it even further. The analysis of full inter-well motion is based on dashed areas 5.1, 5.2, and 5.3 displayed in Figure 33. Tables 6 to 8 summarizes the information regarding the points analyzed in this subsection for each case.

Table 4. Points details of Figure 31.

Point	Response	(Ω, γ)	Inter-well motion	P_{out}
1	Chaotic	(0.932, 0.277)	27.6%	17.17×10^{-3}
2	Chaotic	(0.94, 0.252)	20.4%	16.5×10^{-3}
3	Period-5	(0.979, 0.252)	20%	17.13×10^{-3}
4	Chaotic	(1.0, 0.237)	17.8%	15.87×10^{-3}

Table 5. Points details of Figure 32.

Point	Response	(Ω, γ)	Inter-well motion	P_{out}
1	Chaotic	(1.68, 0.99)	26.6%	21×10^{-3}
2	Chaotic	(1.77, 0.89)	18%	19.52×10^{-3}
3	Period-3	(1.95, 0.89)	33.2%	22.2×10^{-3}

Figure 34 shows zoomed area 5.1. It is a very complex region containing a great diversity of dynamical responses. In this case, comparing points 1 and 2, there is almost no change in power output as period-3 changes to period-1. On the other hand, by comparing points 3 and 4, a small decrease in power output occurs as period-3 changes to period-1. Point 5 exemplifies a chaotic region that presents considerable fluctuations in power output. The abrupt change to chaotic to period-4/period-2 zone represents a great change in the power output. However, period-4 and period-2 present similar power outputs. Period-1 zone, represented by point 8, also displays similar power output as period-4 and period-2 zones, represented by points 6 and 7. Yet,

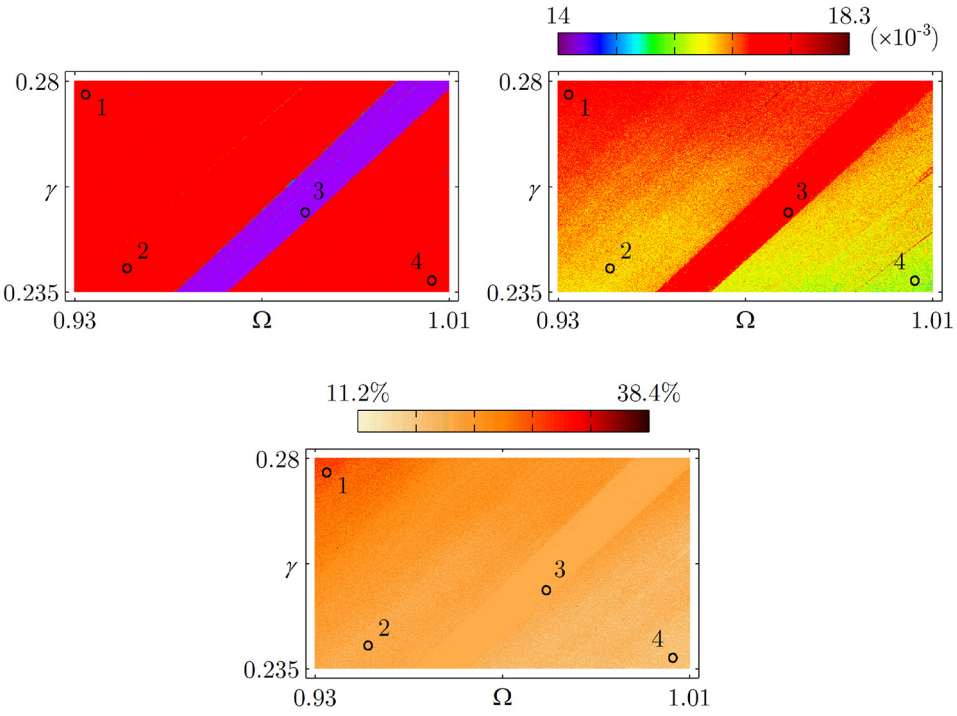

Figure 31. Dynamical response (top left), output power (top right) and inter-well motion (bottom) maps as a function of Ω and γ for $(\alpha, \beta) = (-0.7, 0.25)$ at zoomed area 3 (see Figure 28).

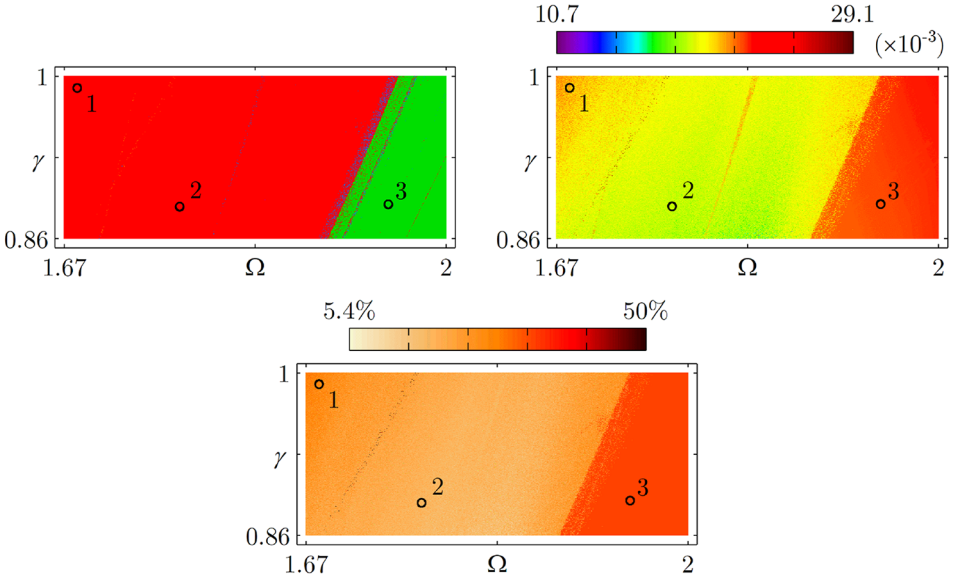

Figure 32. Dynamical response (top left), output power (top right) and inter-well motion (bottom) maps as a function of Ω and γ for $(\alpha, \beta) = (-0.7, 0.25)$ at zoomed area 4 (see Figure 28).

the transition between those regions shows a small abrupt change in power output.

Now analyzing region 5.2, Figure 35 displays another complex region. Point 1 represents the chaotic region, presenting again considerable fluctuations of power output. An abrupt change from chaotic to period-5 region, represented by point 2, increase the power output of the system. However, the abrupt change from chaotic to period-2 response, represented by point 3, decreases the power output of the system.

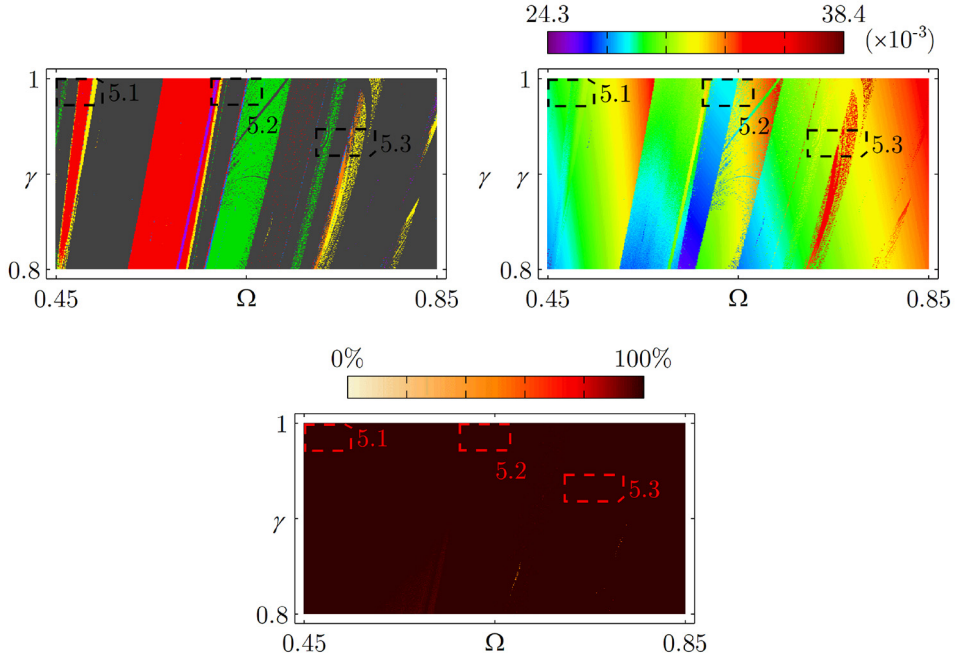

Figure 33. Dynamical response (top left), output power (top right) and inter-well motion (bottom center) maps as a function of Ω and γ for $(\alpha, \beta) = (-0.7, 0.25)$ at zoomed area 5 (see Figure 28).

Table 6. Points details of Figure 34.

Point	Response	(Ω, γ)	P_{out}
1	Period-3	(0.451, 0.993)	28.58×10^{-3}
2	Period-1	(0.452, 0.983)	28.58×10^{-3}
3	Period-3	(0.46, 0.996)	29.08×10^{-3}
4	Period-1	(0.462, 0.985)	28.95×10^{-3}
5	Chaotic	(0.485, 0.99)	29.93×10^{-3}
6	Period-4	(0.487, 0.985)	30.25×10^{-3}
7	Period-2	(0.491, 0.995)	30.42×10^{-3}
8	Period-1	(0.495, 0.989)	30.03×10^{-3}

Table 7. Points details of Figure 35.

Point	Response	(Ω, γ)	P_{out}
1	Chaotic	(0.616, 0.997)	30.05×10^{-3}
2	Period-5	(0.618, 0.99)	31.94×10^{-3}
3	Period-2	(0.622, 0.989)	27.89×10^{-3}
4	Period-1	(0.64, 0.99)	28.14×10^{-3}
5	Period-6 +	(0.649, 0.985)	31.62×10^{-3}
6	Period-3	(0.654, 0.99)	31.8×10^{-3}

Still, period-5 area shows greater power outputs than period-2 response area. In this case, point 4 (period-1 response) represents the lower power achieved. Points 5 and 6, representing period-6 + and period-3 responses, shows almost no variation in power output. In addition, along with period-5 region, these three regions present the best power outputs for this case.

Table 8. Points details of Figure 36.

Point	Response	(Ω, γ)	P_{out}
1	Period-3	(0.735, 0.931)	30.84×10^{-3}
2	Period-1	(0.748, 0.93)	30.53×10^{-3}
3	Chaotic	(0.751, 0.916)	34.75×10^{-3}
4	Period-6 +	(0.753, 0.92)	34.86×10^{-3}
5	Period-4	(0.7595, 0.931)	35.2×10^{-3}
6	Period-2	(0.767, 0.925)	35.58×10^{-3}

Next consider area 5.3, represented in Figure 36. In this case, the abrupt change from period-3 zone (point 1) to period-1 zone (point 2) shows a small drop in power output. While the abrupt change for period-1 zone to chaotic/period-6 + /period-4/period-2 zones (points 3, 4, 5, and 6) cause a large increase in power. In addition, these zones represented by points 3, 4, 5, and 6 have almost no variation in power by dynamical response transition. In this case is also very clear the presence of an erosion of regions, associated with fractal-like structures.

Summarizing this section, it should be pointed out that, for intra-well motions, changes in the dynamical response might result in relative large fluctuations in power output of the system. On the other hand, for full inter-well motions, changes in the dynamical response can cause relative small changes in power output. Still, for cases showing partial inter-well motions, its intensity (percentage of inter-well motion) exerts much more

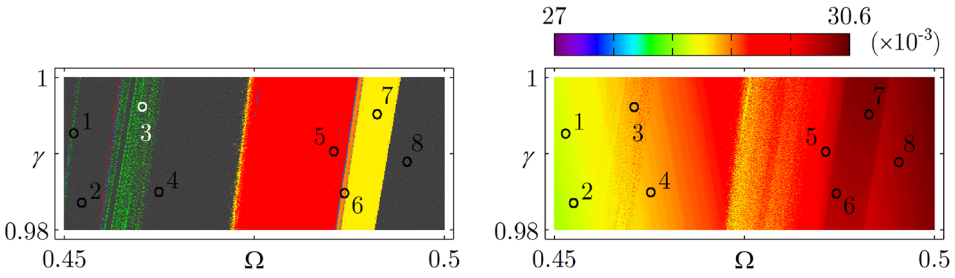

Figure 34. Dynamical response (left) and output power (right) maps as a function of Ω and γ for $(\alpha, \beta) = (-0.7, 0.25)$ at zoomed area 5.1 (see Figure 33).

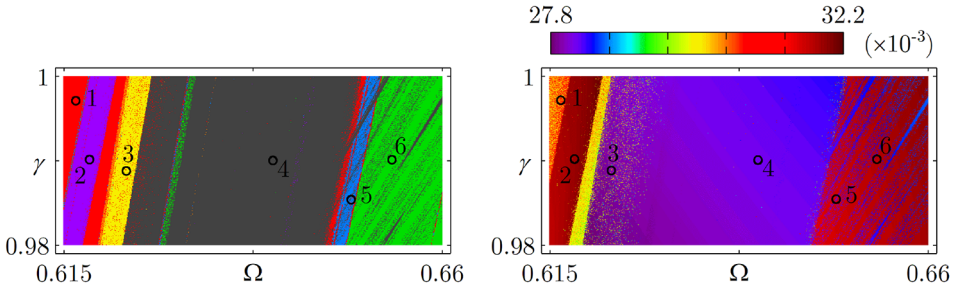

Figure 35. Dynamical response (left) and output power (right) maps as a function of Ω and γ for $(\alpha, \beta) = (-0.7, 0.25)$ at zoomed area 5.2 (see Figure 33).

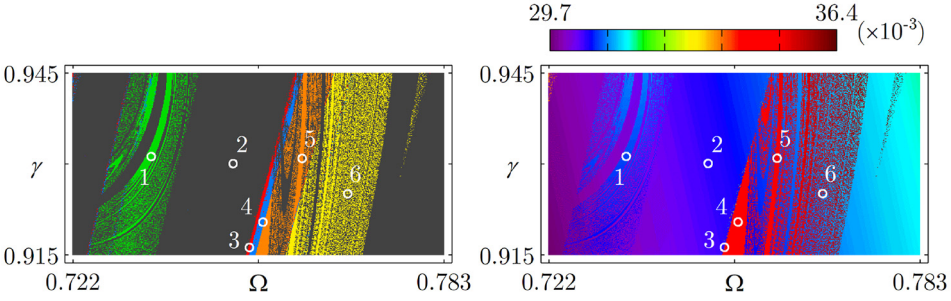

Figure 36. Dynamical response (left) and output power (right) maps as a function of Ω and γ for $(\alpha, \beta) = (-0.7, 0.25)$ at zoomed area 5.3 (see Figure 33).

influence than dynamic response abrupt changes. Figures 37 to 39 show dynamical response, output power and inter-well occurrence intensity ($IW(\%)$) bifurcation diagrams illustrating even further these behaviors. Two parameter cases are chosen, representing a best case scenario region for output power ($\alpha = -0.7, \beta = 0.25$) and a best case scenario bandwidth region ($\alpha = -0.65, \beta = 2$). The bifurcations use the same initial condition for each step, as described in Table 1, and Poincaré sections are employed to distinguish dynamical responses. Note that power output drops almost proportionally when there is a change of full inter-well motion to partial inter-well motion; and drops even more when there is a change of partial inter-well motion to intra-well motion. Changes in dynamical response slightly changes the output power.

8. Conclusion

This work deals with a deep dynamical investigation of bistable piezoelectric energy harvesting systems modeled with a cubic nonlinearity. Numerical procedures are employed to perform a parametric analysis regarding the stiffness and excitation parameters. Simulations are carried out in order to qualitatively predict the performance of these generators.

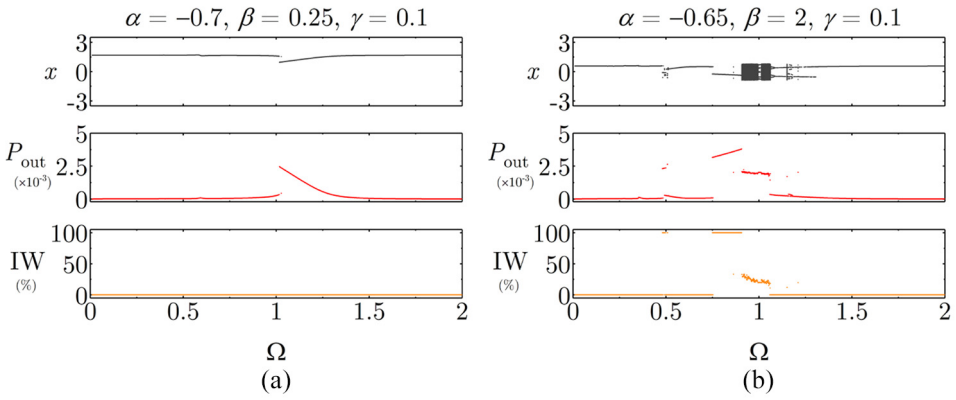

Figure 37. Bifurcation diagrams for dynamical response, output power and percentage of inter-well motion with $\gamma = 0.1$ for: (a) best case scenario power output case ($\alpha = -0.7, \beta = 0.25$), and (b) best case scenario bandwidth case ($\alpha = -0.65, \beta = 2$).

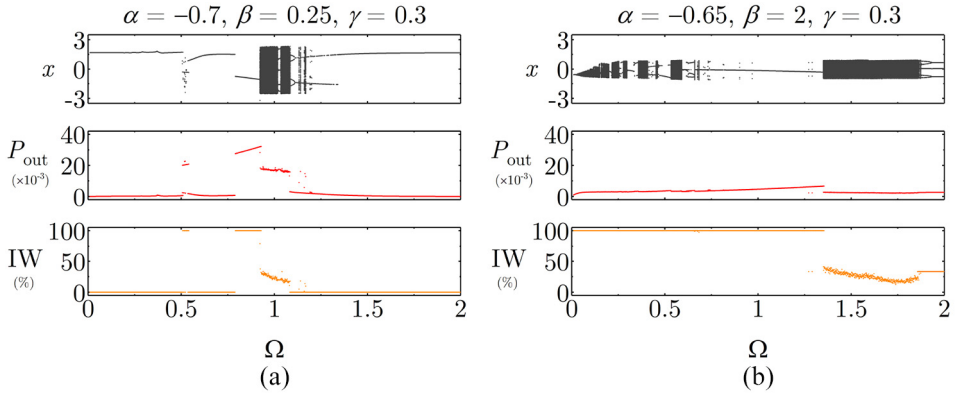

Figure 38. Bifurcation diagrams for dynamical response, output power and percentage of inter-well motion with $\gamma = 0.3$ for: (a) best case scenario power output case ($\alpha = -0.7, \beta = 0.25$), and (b) best case scenario bandwidth case ($\alpha = -0.65, \beta = 2$).

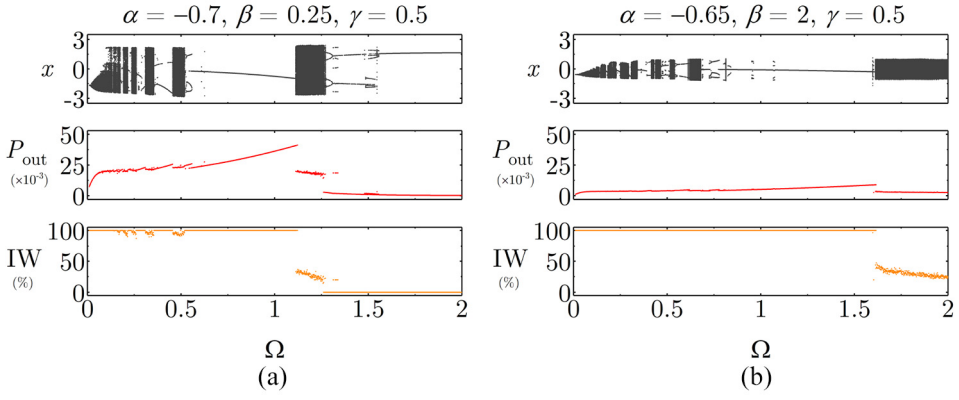

Figure 39. Bifurcation diagrams for dynamical response, output power and percentage of inter-well motion with $\gamma = 0.5$ for: (a) best case scenario power output case ($\alpha = -0.7, \beta = 0.25$), and (b) best case scenario bandwidth case ($\alpha = -0.65, \beta = 2$).

Dynamical analysis shows that the system can present a great variety of dynamical response patterns that are intrinsic to the system, also showing fractal-like structures. Dynamical response maps as function of stiffness parameters show that the increase of excitation frequency makes such patterns to present an expansion and translate to the top of the map (from lower to higher values of β). On the other hand, the increase of

excitation amplitude makes the patterns to exhibit a contraction and move to the bottom of the map (from higher to lower values of β). Also, the most prominent dynamical responses are period-1, chaotic, period-3, and period-2, respectively. Period-4, period-5, and period-6 or more are less likely to occur. The transition between dynamical responses may result in relatively small changes to power output, however the best overall dynamical response has not been identified.

Potential energy analysis shows that the system can exhibit intra-well motion, partial and full inter-well motions. The trigger of inter-well motion is associated with a large increase in power output. The greater is the intensity of inter-well motion, the greater is the power output. Besides, the combination of stiffness parameters presenting a low potential energy barrier is likely to exhibit more complex dynamics and larger bandwidth operation. The best areas for larger bandwidths and small base forcing magnitude to trigger inter-well motion present lower power conversion, while higher power outputs are likely to occur for higher values of stiffness parameters, presenting median bandwidths. The best efficiencies also occur for higher values of stiffness coefficient combined with low values of nonlinear stiffness coefficient. It is also observed that the combination of parameters that increases the chance of the system of generating higher power outputs have a trend to be more efficient.

Regarding the excitation parameters, the increase in excitation amplitude results in the occurrence of maximum power output at higher frequencies. Moreover, it is observed an increase in power output for higher values of excitation amplitude. On the other hand, low values of excitation amplitude make the system more efficient.

Concluding, a relation between the shape of the potential energy curve and different characteristics of interest for energy harvesting are established in order to identify the best configurations and enhance the efficiency and power output of bistable piezoelectric energy harvesting systems for different situations.

Acknowledgements

The authors would like to acknowledge the support of the Brazilian Research Agencies CNPq, CAPES, and FAPERJ.

Declaration of conflicting interests

The author(s) declared no potential conflicts of interest with respect to the research, authorship, and/or publication of this article.

Funding

The author(s) received no financial support for the research, authorship, and/or publication of this article.

ORCID iDs

Luã Guedes Costa https://orcid.org/0000-0002-2836-723X
Pedro Manuel Calas Lopes Pacheco https://orcid.org/0000-0002-3374-5119
Marcelo Amorim Savi https://orcid.org/0000-0001-5454-5995

References

Ai R, Monteiro LLS, Monteiro PCC, et al. (2019) Piezoelectric vibration-based energy harvesting enhancement exploiting nonsmoothness. *Actuators* 8(1): 25.

Andò B, Baglio S, Trigona C, et al. (2010) Nonlinear mechanism in MEMS devices for energy harvesting applications. *Journal of Micromechanics and Microengineering* 20(12): 125020.

Blystad L-CJ and Halvorsen E (2011) A piezoelectric energy harvester with a mechanical end stop on one side. *Microsystem Technologies* 17(4): 505–511.

Cellular AC, da Silva Monteiro LL and Savi MA (2018) Numerical investigation of nonlinear mechanical and constitutive effects on piezoelectric vibration-based energy harvesting. *Technisches Messen* 85(9): 565–579.

Cottone F, Gammaitoni L, Vocca H, et al. (2012) Piezoelectric buckled beams for random vibration energy harvesting. *Smart Materials and Structures* 21(3): 035021.

duToit NE, Wardle BL and Kim S-G (2005) Design considerations for mems-scale piezoelectric mechanical vibration energy harvesters. *Integrated Ferroelectrics* 71(1): 121–160.

Erturk A, Hoffmann J and Inman DJ (2009) A piezomagnetoelastic structure for broadband vibration energy harvesting. *Applied Physics Letters* 94(25): 254102.

Erturk A and Inman D (2011a) Broadband piezoelectric power generation on high-energy orbits of the bistable duffing oscillator with electromechanical coupling. *Journal of Sound and Vibration* 330(10): 2339–2353.

Erturk A and Inman DJ (2008) Issues in mathematical modeling of piezoelectric energy harvesters. *Smart Materials and Structures* 17(6): 065016.

Erturk A. and Inman DJ (2011b) *Piezoelectric Energy Harvesting*. Hoboken, NJ: John Wiley & Sons, Inc.

Ferrari M, Ferrari V, Guizzetti M, et al. (2010) Improved energy harvesting from wideband vibrations by nonlinear piezoelectric converters. *Sensors and Actuators A: Physical* 162(2): 425–431.

Haitao L, Weiyang Q, Chunbo L, et al. (2015) Dynamics and coherence resonance of tri-stable energy harvesting system. *Smart Materials and Structures* 25(1): 015001.

Kim JE and Kim YY (2011) Analysis of piezoelectric energy harvesters of a moderate aspect ratio with a distributed tip mass. *Journal of Vibration and Acoustics* 133(4): 041010.

Kim M, Hoegen M, Dugundji J, et al. (2010) Modeling and experimental verification of proof mass effects on vibration energy harvester performance. *Smart Materials and Structures* 19(4): 045023.

Kim P and Seok J (2014) A multi-stable energy harvester: dynamic modeling and bifurcation analysis. *Journal of Sound and Vibration* 333(21): 5525–5547.

Kim P and Seok J (2015) Dynamic and energetic characteristics of a tri-stable magnetopiezoelastic energy harvester. *Mechanism and Machine Theory* 94: 41–63.

Kumar KA, Ali SF and Arockiarajan A (2015) Piezomagnetoelastic broadband energy harvester: nonlinear modeling and characterization. *The European Physical Journal Special Topics* 224(14): 2803–2822.

Kumar KA, Ali SF and Arockiarajan A (2017) Magneto-elastic oscillator: modeling and analysis with nonlinear magnetic interaction. *Journal of Sound and Vibration* 393: 265–284.

Lin J-T and Alphenaar B (2010) Enhancement of energy harvested from a random vibration source by magnetic coupling of a piezoelectric cantilever. *Journal of Intelligent Material Systems and Structures* 21(13): 1337–1341.

Liu H, Lee C, Kobayashi T, et al. (2012) Investigation of a MEMS piezoelectric energy harvester system with a frequency-widened-bandwidth mechanism introduced by mechanical stoppers. *Smart Materials and Structures* 21(3): 035005.

Liu W, Formosa F, Badel A, et al. (2016) Investigation of a buckled beam generator with elastic clamp boundary. *Smart Materials and Structures* 25(11): 115045.

Liu W, Formosa F, Badel A, et al. (2017) A simplified lumped model for the optimization of post-buckled beam architecture wideband generator. *Journal of Sound and Vibration* 409: 165–179.

Liu WQ, Badel A, Formosa F, et al. (2013) Novel piezoelectric bistable oscillator architecture for wideband vibration energy harvesting. *Smart Materials and Structures* 22(3): 035013.

Masana R and Daqaq MF (2011) Relative performance of a vibratory energy harvester in mono- and bi-stable potentials. *Journal of Sound and Vibration* 330(24): 6036–6052.

Moon F and Holmes P (1979) A magnetoelastic strange attractor. *Journal of Sound and Vibration* 65(2): 275–296.

Paula ASD, Inman DJ and Savi MA (2015) Energy harvesting in a nonlinear piezomagnetoelastic beam subjected to random excitation. *Mechanical Systems and Signal Processing* 54: 405–416.

Qian F, Zhou S and Zuo L (2020) Approximate solutions and their stability of a broadband piezoelectric energy harvester with a tunable potential function. *Communications in Nonlinear Science and Numerical Simulation* 80: 104984.

Sebald G, Kuwano H, Guyomar D, et al. (2011) Experimental duffing oscillator for broadband piezoelectric energy harvesting. *Smart Materials and Structures* 20(10): 102001.

Sneller AJ, Cette P and Mann BP (2011) Experimental investigation of a post-buckled piezoelectric beam with an attached central mass used to harvest energy. *Proceedings of the Institution of Mechanical Engineers, Part I: Journal of Systems and Control Engineering* 225(4): 497–509.

Stanton SC, McGehee CC and Mann BP (2010) Nonlinear dynamics for broadband energy harvesting: investigation of a bistable piezoelectric inertial generator. *Physica D: Nonlinear Phenomena* 239(10): 640–653.

Stanton SC, Owens BA and Mann BP (2012) Harmonic balance analysis of the bistable piezoelectric inertial generator. *Journal of Sound and Vibration* 331(15): 3617–3627.

Toprak A and Tigli O (2014) Piezoelectric energy harvesting: state-of-the-art and challenges. *Applied Physics Reviews* 1(3): 031104.

Tran N, Ghayesh MH and Arjomandi M (2018) Ambient vibration energy harvesters: a review on nonlinear techniques for performance enhancement. *International Journal of Engineering Science* 127: 162–185.

Wang C, Zhang Q, Wang W, et al. (2018a) A low-frequency, wideband quad-stable energy harvester using combined nonlinearity and frequency up-conversion by cantilever-surface contact. *Mechanical Systems and Signal Processing* 112: 305–318.

Wang W, Cao J, Bowen CR, et al. (2018b) Multiple solutions of asymmetric potential bistable energy harvesters: numerical simulation and experimental validation. *The European Physical Journal B* 91: 254.

Wolf A, Swift JB, Swinney HL, et al. (1985) Determining lyapunov exponents from a time series. *Physica D: Nonlinear Phenomena* 16(3): 285–317.

Yildirim T, Ghayesh MH, Li W, et al. (2017) A review on performance enhancement techniques for ambient vibration energy harvesters. *Renewable and Sustainable Energy Reviews* 71: 435–449.

Zhou S, Cao J, Erturk A, et al. (2013) Enhanced broadband piezoelectric energy harvesting using rotatable magnets. *Applied Physics Letters* 102(17): 173901.

Zhou S, Cao J, Inman DJ, et al. (2014) Broadband tristable energy harvester: modeling and experiment verification. *Applied Energy* 133: 33–39.

Zhou Z, Qin W, Yang Y, et al. (2017a) Improving efficiency of energy harvesting by a novel penta-stable configuration. *Sensors and Actuators A: Physical* 265: 297–305.

Zhou Z, Qin W and Zhu P (2017b) A broadband quad-stable energy harvester and its advantages over bi-stable harvester: simulation and experiment verification. *Mechanical Systems and Signal Processing* 84: 158–168.

Zhu P, Ren X, Qin W, et al. (2017) Improving energy harvesting in a tri-stable piezomagnetoelastic beam with two attractive external magnets subjected to random excitation. *Archive of Applied Mechanics* 87(1): 45–57.